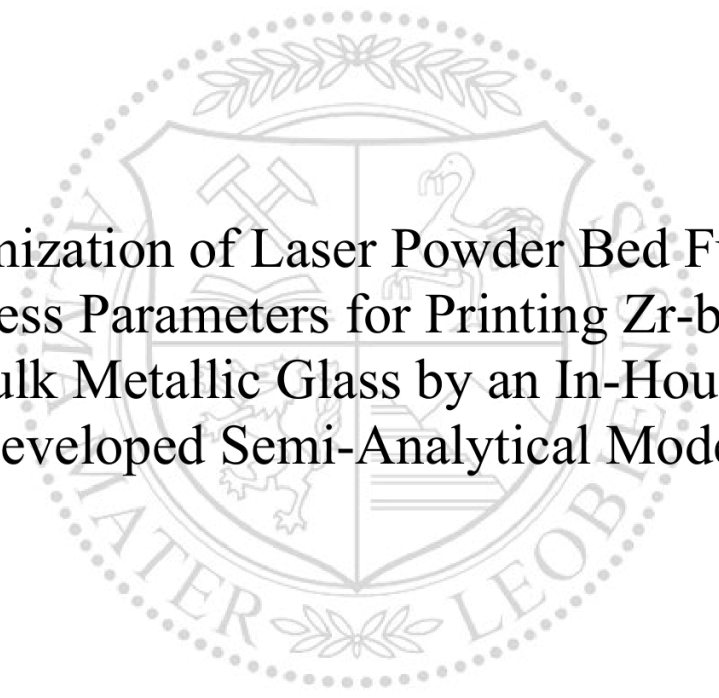




Chair of Metal Forming

Master's Thesis



Optimization of Laser Powder Bed Fusion
Process Parameters for Printing Zr-based
Bulk Metallic Glass by an In-House
Developed Semi-Analytical Model

Emanuel Gingl

October 2023



MONTANUNIVERSITÄT LEOBEN
www.unileoben.ac.at

EIDESSTÄTTLICHE ERKLÄRUNG

Ich erkläre an Eides statt, dass ich diese Arbeit selbständig verfasst, andere als die angegebenen Quellen und Hilfsmittel nicht benutzt, und mich auch sonst keiner unerlaubten Hilfsmittel bedient habe.

Ich erkläre, dass ich die Richtlinien des Senats der Montanuniversität Leoben zu "Gute wissenschaftliche Praxis" gelesen, verstanden und befolgt habe.

Weiters erkläre ich, dass die elektronische und gedruckte Version der eingereichten wissenschaftlichen Abschlussarbeit formal und inhaltlich identisch sind.

Datum 16.10.2023

Unterschrift Verfasser/in
Emanuel Gingl

Acknowledgements

I would like to express my deepest gratitude to Prof. Eckert Jürgen and Dr. Florian Spieckermann for their unwavering support, guidance, and encouragement throughout my thesis journey. Their expertise and insight have been invaluable in shaping this work.

I am also grateful to Dipl.-Ing. Sepide Hadibeik Neishaboori for their constructive feedback, insightful comments, and valuable suggestions. Her expertise in the field has been immensely helpful in refining my research and improving the quality of this thesis.

I extend my heartfelt thanks to all my colleagues at the Erich Schmid Institute who generously contributed their time and resources to my project. Their assistance and support were critical to the successful completion of my research.

I am indebted to my parents, Manfred and Karin, as well as my girlfriend, Victoria, who provided unwavering support, encouragement, and motivation during this challenging period. Their presence and care provided a much-needed source of inspiration and motivation.

Finally, I would like to thank all the participants who took part in my research, without whom this study would not have been possible. Your contributions have been invaluable, and I am grateful for your time and effort.

Thank you all for your contributions to this thesis.

Abstract

Laser powder bed fusion (LPBF) is a revolutionary technology that has recently been recognized as an ideal manufacturing method for Zr-based bulk metallic glasses (BMGs). Current state-of-the-art manufacturing methods such as arc-melting, and copper mold casting, have limitations in realizing complex geometries, while LPBF offers more flexibility. Moreover, LPBF allows for a fine balance between the generation of intricate features and maintaining appropriate cooling rates throughout the process.

This study focuses on the optimization of process parameters of a particular, additively manufactured Zr-based alloy, AMZ4, due to its superior qualities and commercial availability, with the goal to improve its mechanical and thermal properties. A preliminary parameter selection analysis is carried out, revealing the relationship between energy density and porosity. Several experiments, including dynamic mechanical analysis (DMA), differential scanning calorimetry (DSC), and scanning electron microscopy (SEM), are subsequently conducted on the samples manufactured by LPBF. Valuable insight is gained regarding the glass transformation characteristics, β -relaxation behavior, and microstructure of the samples. An in-house developed, semi-analytical simulation algorithm is created to calculate the thermal history for single-track, as well as multi-track, multi-layer LPBF simulations. The model is coupled with a function which evaluates the degree of crystallinity using the forward Euler method, providing vital information regarding presence of crystal phases within the microstructure. This allows for a significant reduction in the amount of required time-intensive laboratory experiments.

Of the ten samples tested, the study finds that energy densities of less than 50J/mm^3 are required to achieve optimal thermal stability and that energy densities lower than 40J/mm^3 increase amorphous content. The outcomes support the theoretical claims that lower energy densities lead to increased amorphous content, which in turn leads to improved mechanical properties including ductility. The work concludes that Zr-based BMGs are promising engineering materials with potential applications in the medical industry, and additive manufacturing methods like LPBF can enhance the BMG manufacturing process by allowing for the generation of intricate features and maintaining appropriate cooling rates. The research findings aim to contribute to the broader applicability of AMZ4 and accelerate the development of similar advanced engineering materials.

Kurzfassung

Laserstrahlschmelzen (englisch: Laser Powder Bed Fusion, LPBF) ist eine revolutionäre Technologie, die in jüngster Zeit als ideale Herstellungsmethode für massive metallische Gläser auf Zr-Basis (englisch: bulk metallic glasses, BMG) anerkannt wurde. Die derzeit modernsten Herstellungsverfahren, das Lichtbogenschmelzen und der Kupferformguss, sind bei der Realisierung komplexer Geometrien eingeschränkt, während das additive LPBF mehr Flexibilität bietet. Darüber hinaus ermöglicht LPBF ein feines Gleichgewicht zwischen der Erzeugung feiner Details und der Aufrechterhaltung angemessener Kühlraten während des gesamten Prozesses.

Diese Studie konzentriert sich auf die Optimierung der Prozessparameter einer bestimmten, additiv hergestellten Zr-Basislegierung, AMZ4, aufgrund ihrer überlegenen Eigenschaften und ihrer kommerziellen Verfügbarkeit, mit dem Ziel, ihre mechanischen und thermischen Eigenschaften zu verbessern. Es wird eine vorläufige Analyse der Parameterauswahl durchgeführt, die die Beziehung zwischen Energiedichte und Porosität aufzeigt. Anschließend werden mehrere Experimente, darunter die dynamisch-mechanische Analyse (DMA), die dynamische Differenzkalorimetrie (englisch: differential scanning calorimetry, DSC) und die Rasterelektronenmikroskopie (SEM), an einer reduzierten Probengröße durchgeführt. Es werden wertvolle Erkenntnisse über die Glasumwandlungseigenschaften, das β -Relaxationsverhalten und die Mikrostruktur der Proben gewonnen. Mittels eines selbst entwickelten, halbanalytischen Simulationsalgorithmus, werden die thermischen Abläufe für einspurige sowie mehrspurige, mehrschichtige LPBF-Simulationen berechnet. Das Modell ist mit einer Funktion gekoppelt, die den Kristallinitätsgrad mit Hilfe des Euler-vorwärts-Verfahrens auswertet und so wichtige Informationen über das Vorhandensein von Kristallphasen in der Mikrostruktur liefert. Auf diese Weise lässt sich der Umfang der erforderlichen zeitintensiven Laborexperimente erheblich verringern.

Anhand der zehn getesteten Proben zeigt die Studie, dass Energiedichten von weniger als 50J/mm^3 erforderlich sind, um eine optimale thermische Stabilität zu erreichen, und dass Energiedichten von weniger als 40J/mm^3 den amorphen Anteil erhöhen. Die Ergebnisse stützen die theoretischen Behauptungen, dass niedrigere Energiedichten zu einem höheren amorphen Anteil führen, was wiederum zu verbesserten mechanischen Eigenschaften einschließlich der Duktilität führt. Die Arbeit kommt zu dem Schluss, dass BMGs auf Zr-Basis vielversprechende technische Werkstoffe mit potenziellen Anwendungen in der Medizinindustrie darstellen und dass additive Fertigungsverfahren wie LPBF den BMG-Fertigungsprozess verbessern können, indem sie die Erzeugung feiner Strukturen und die Aufrechterhaltung angemessener Kühlraten ermöglichen. Die Forschungsergebnisse sollen zu einer breiteren Anwendbarkeit von AMZ4 beitragen und die Entwicklung ähnlicher fortschrittlicher Materialien beschleunigen.

Contents

1	LIST OF ABBREVIATIONS	8
2	INTRODUCTION	9
2.1	Aim of the Work	9
3	THEORETICAL BACKGROUND	10
3.1	Bulk Metallic Glasses (BMGs)	10
3.2	AMZ4	12
3.3	Laser Powder Bed Fusion (LPBF)	13
3.4	Crystallization of Zr-based BMGs	15
3.5	Nucleation and Growth	19
4	METHODS AND MATERIALS	21
4.1	Laser Powder Bed Fusion (LPBF)	21
4.2	Scanning Electron Microscopy (SEM)	22
4.3	Differential Scanning Calorimetry (DSC)	22
4.4	Dynamic Mechanical Analysis (DMA)	23
4.5	Semi-Analytical Modeling	24
4.5.1	State of the Art	24
4.5.2	Model Implementation	26
5	RESULTS	33
5.1	Parameter Selection Study	33
5.2	SEM	36
5.3	LPBF Simulation	38
5.4	DSC	43

5.5	DMA	47
6	DISCUSSION	50
6.1	Relaxation	50
6.2	Model Validation	51
6.3	Parameter Optimization	55
7	CONCLUSION	57
8	REFERENCES	59
9	APPENDIX	64
9.1	Linearization of C_p	64
9.2	Single-Track Model	65
9.3	Single-Track Validation	68
9.4	Multi-Track Model	71
9.5	Nakamura Function	75

1 List of Abbreviations

AI	Artificial Intelligence
BMG	Bulk Metallic Glass
CNT	Classical Nucleation Theory
DMA	Dynamic Mechanical Analysis
DSC	Differential Scanning Calorimetry
E'	Storage Modulus
E''	Loss Modulus
FEM	Finite Element Method
GFA	Glass-Forming Ability
HAZ	Heat Affected Zone
JMAK	Johnson-Mehl-Avrami-Kolgomorov
LPBF	Laser Powder Bed Fusion
ML	Machine Learning
OM	Optical Microscopy
SEM	Scanning Electron Microscopy
T _g	Glass Transition Temperature
TPF	Thermoplastic Forming
TTT	Time-Temperature Transformation
T _x	Crystallization Temperature
XRD	X-Ray Diffraction

2 Introduction

Bulk metallic glasses (BMGs) are becoming increasingly more interesting to the field of materials science as a result of their excellent mechanical as well as molecular properties. Essentially, they are formed from three or more metals, and are amorphous, otherwise known as non-crystalline in nature. [1] This is exactly what differentiates them from ordinary metals, which are crystalline. The atomic arrangement is thus disordered. This results in the absence of crystalline defects such as grain boundaries or dislocations. This characteristic allows for BMGs to exhibit high mechanical strength, good fracture toughness and a low modulus of elasticity. [2] As a result, researchers around the world are looking for a way to better understand, manufacture and make use of these materials in for example, the medical field.

In order to broaden the applicability of these materials, considerable modifications must be made to the available manufacturing processes. The current state of the art is such that BMGs are typically manufactured via arc-melting and copper mold casting. Although these conventional methods have been proven effective, a significant drawback is that complex geometries cannot be realized easily [3]. This is the advantage of additive manufacturing, which allows for a fine balance between the generation of intricate features and maintaining appropriate cooling rates throughout the duration of the process. One of the most common additive manufacturing methods for this application is LPBF. Essentially, a laser is responsible for joining a powder by fusing it layer by layer in accordance with the desired geometry obtained from CAD data. [4]

Since 1960, researchers from various academic institutions have collaborated on the development of several different types of BMGs including Zr-, Ti-, Cu-, Fe-, Ni-, Cu-, and Pd-, based alloys. [5] Due to its superior qualities, such as an excellent glass forming ability, and commercial availability, this investigation will mainly deal with a particular Zr-based alloy, defined by its trade name as AMZ4. [6]

2.1 Aim of the Work

The aim of the study carried out in this master's thesis is to gain a better understanding of the underlying physical processes during additive manufacturing of AMZ4. Additionally, the process parameters are to be optimized in order to improve mechanical and thermal properties including ductility and thermal stability. Several different sets of samples are manufactured using LPBF with variations in the laser power and the scanning speed. A preliminary parameter selection study

based on sample density is followed by a series of experiments including dynamic mechanical analysis (DMA), differential scanning calorimetry (DSC) and scanning electron microscopy (SEM). Using an internally developed algorithm, semi-analytical simulations were carried out to help estimate the presence of crystal phases within the microstructure. Additionally, this study discusses how the optimized process parameters are connected to the physical parameters, as reviewed in the literature and within the scope of this research. These insights are then considered in terms of their potential application in structural materials.

3 Theoretical Background

3.1 Bulk Metallic Glasses (BMGs)

Bulk metallic glasses, are relatively new to the field of metallurgy, having first been discovered in 1960 by Klement et al. In the study, an Au-Si alloy was rapidly quenched from its molten state using a self-made apparatus. Analysis via X-Ray diffraction (XRD) revealed the presence of an amorphous structure. It was thus speculated that many other, if not all alloys may have the ability to form amorphous structures, provided the processing conditions such as cooling rates during solidification are appropriate. [7]

Since then, considerable efforts have been made concerning the research and development of BMGs. The investigation of amorphous alloys is driven by their impressive mechanical properties, including exhibiting similar elastic moduli to conventional engineering metals whilst offering room-temperature strengths superior to those of polycrystalline materials with comparable compositions. Exceptional hardness, along with wear and corrosion resistance are typically also to be expected. Despite their tendency for shear localization and macroscopically brittle failure, there is evidence that metallic glasses are capable of plastic shear flow at the microscale, offering high strength with non-negligible toughness. Research efforts have focused on the room-temperature properties of metallic glasses, while their amorphous structure enables stable Newtonian flow at low stresses, low strain rates or elevated temperatures, allowing for superplastic-like deformation useful in shape-forming operations. [8, 9, 10]

To better understand the mechanical behavior of BMGs, it is necessary to assess them on an atomic level as amorphous solids. The atomic arrangement is disordered and lacks long-range order, meaning that the positions of the atoms are disordered and have no periodically repeating

pattern. Obtaining such a degree of disorder in the atomic arrangement is greatly dependent on the atomic sizes, as a substantial difference in atomic radii among the constituents can result in a higher level of randomness in the atomic arrangement. Moreover, a lack of long-range order leads to an increase in homogeneity within the material, resulting in an absence of point defects, dislocations, as well as stacking faults. In contrast, crystalline solids have a highly ordered and repetitive atomic arrangement, which results in the formation of a crystal lattice. The atoms in a crystal are arranged in a specific geometric pattern, which repeats throughout the solid in all three dimensions. To summarize, BMG's are often times preferred over crystalline materials largely due to the characteristics of their atomic structures. [11]

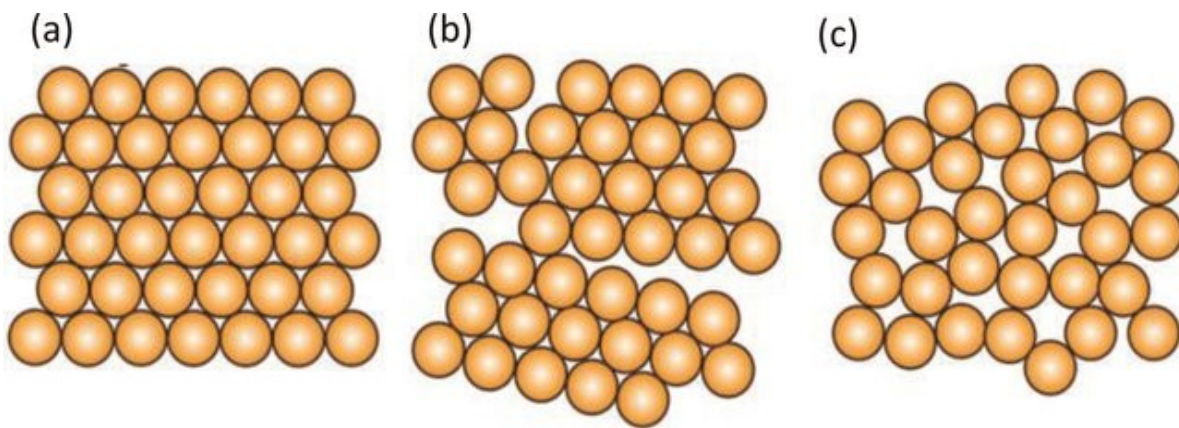


Figure 1: A comparison between the arrangement of a) single crystal structure b) polycrystalline structure and c) amorphous structure [11]

Selecting suitable manufacturing methods for the fabrication of BMGs is a difficult task considering the tolerances associated with the narrow processing window as discussed in the upcoming sections. It is therefore common to opt for direct casting and metal spinning, in which cooling and forming take place simultaneously. The disadvantage in this case is, however, the ability to produce intricate geometries because of the inherent demand to maintain a high enough cooling rate. An alternative would be to consider thermoplastic forming (TPF), which allows for processing of the desired alloy just above its respective glass transition temperature (T_g). Taking advantage of the relatively low viscosity exhibited in the supercooled liquid region, the required geometry can be shaped with ease in isothermal conditions. Methods that fall into this category include but are not limited to injection molding, wire drawing, extrusion and blow molding. [9] Despite the apparent benefits of TPF, a new challenge arises, in that the desired decrease in viscosity is inversely proportional to an increase in temperature, leading to longer cooling times, and subsequently, unintended crystallization. [12] A compromise between viscosity and crystallization time is consequently necessary. Due to the advancement of technology, a third method for BMG

processing can be considered, namely laser based additive manufacturing. The short interaction time between the laser and the material in conjunction with the small volume that is targeted, allows for cooling rates up to 10^3 - 10^8 K/s. [9]

3.2 AMZ4

AMZ4 is the trade name for a Zr-based BMG-forming alloy with a composition in at. % as follows: $Zr_{59.3}Cu_{28.8}Al_{10.4}Nb_{1.5}$. One of the most well-known suppliers of this powder is Heraeus AMLOY Technologies, who provides the material in its well-known powder form. [13] Due to the complexity behind processing such a material, and despite being commercially available, the alloy is still being investigated by many researchers in order to determine ways to further improve its properties. Furthermore, the patent for processing AMZ4 powder was filed as recently as 2018, supporting the fact that this BMG is an up-and-coming material in the field of materials science. [14]

In order to evaluate the applications of such a material manufactured via laser powder bed fusion (LPBF), several mechanical experiments have been conducted in the past few years including impact, tensile, and compression tests, among others. From a set of three tensile tests, it was found that the tensile yield strength varied from approximately 880 ± 88 MPa to 1180 ± 72 MPa. The stress-strain relationship was determined to be linear as a result of a profound lack of plastic deformation. Impact toughness tests were conducted in the same study, leading to a range between 123 ± 28 mJ and 163 ± 21 mJ, with a statistical scatter of the results of around 12%. It is important to note that a variation in the process parameters was at least partially responsible for the skew in the results. [15] Another study which as well deals with determining mechanical properties of the Zr-based alloy, measured Young's modulus via ultrasonic resonance frequency to be 83.3GPa. A 3-point bending test was also performed, yielding a flexural strength of 1666 ± 33 MPa, one of the best results achieved in bending for BMG's manufactured using LPBF. [16]

3.3 Laser Powder Bed Fusion (LPBF)

Laser powder bed fusion is a form of additive manufacturing that has been evolving since the 1990's due to the rapid prototyping demands of many different markets including aerospace, automotive and defense industries. [17] The process begins with a thin layer of the material being evenly distributed across a build plate, after which a high intensity laser beam scans the surface, melting the powder and fusing it to the layer beneath. The movement of this laser is controlled by a system used to deflect the beam, which is comprised of Galvano mirrors, as well as a focusing lens. After completion of a single layer, the build plate is lowered, and the process is repeated with a new layer of powder until the object is complete. In order to prevent surface oxidation, the build takes place in an enclosed chamber containing an inert gas such as nitrogen or argon. Similar to other additive manufacturing methods, the geometry of the finished product is typically in accordance with design data obtained from CAD software. [18] An illustrative overview of this 3D-printing process is given by Figure 2.

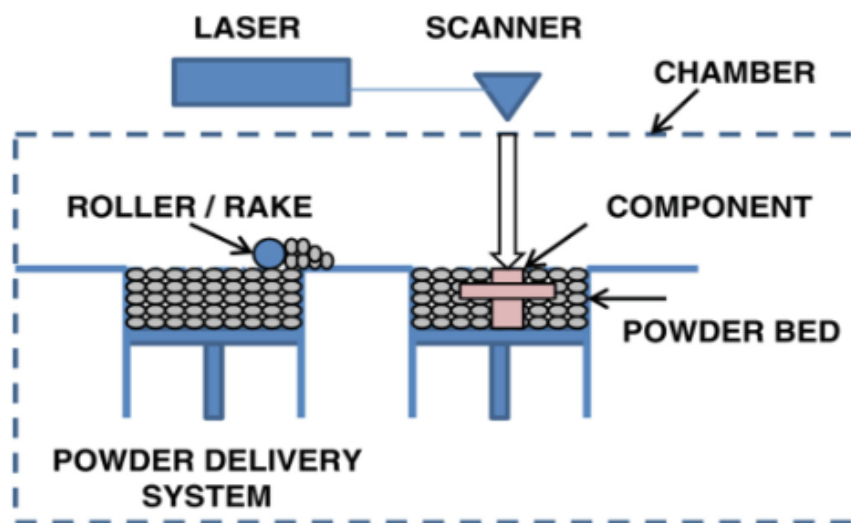


Figure 2: Schematic overview of a typical LPBF process with all relevant components [19]

As the laser scans the workpiece, high cooling rates exceeding 1000K/s may be experienced during melt pool solidification. [18] Due to the influence of the melt pool geometry on the cooling behavior, and in turn, the resulting microstructure of the material, it is vital to consider the thermal field created by the laser beam profile. In most cases, the Gaussian beam profile has been considered the standard for selective laser melting, among other manufacturing processes, in which the temperature distribution steeply decays from the center towards the outer regions.

Recent developments have, however, allowed for so-called beam shaping, which employ static or dynamic methods that permit a manipulation of the beam distribution. [20]

One of the biggest challenges associated with LPBF manufacturing is the risk of generating parts with low density, which in turn, leads to porosity. The presence of pores or voids within a printed part can be problematic as they tend to adversely affect the mechanical properties of the part. Some of the properties that are affected include tensile behavior, impact toughness, fracture toughness, creep response, wear, and fatigue. As an example, in a recent study, the tensile properties of samples with porosities of 0.27, 0.02, and 0.05 were compared. The results showed that the sample with the lowest porosity had an ultimate tensile strength, yield strength, and elongation well over 100% higher than that of the sample with the highest porosity. [21] There are several factors responsible for a lack of density including powder morphology, variations in particle size, packing density, and the quality of the powder itself. In addition to powder characteristics, it is also important to consider the interaction between the laser and the powder when evaluating sample density. For example, it is known that an increase in layer thickness will result in incomplete melting of the previous layer, contributing to lack-of-fusion defects. Therefore, a formula is used to define what is known as the energy density of the laser beam E , as a function of laser power P , scan speed v , hatching distance h , and layer thickness d . [22]

$$E = \frac{P}{vhd} \quad (1)$$

Under the assumption that the layer thickness as well as the hatching distance remain constant, a delicate balance between laser power and scan speed is required in order to fabricate fully dense parts. Another shortcoming of this particular process is the fact that LPBF has the slowest build rate of all additive manufacturing methods that create metal. In order to counter this, recent advancements such as multi-layer concurrent printing have been developed, and in some cases, already implemented. [18]

3.4 Crystallization of Zr-based BMGs

One of the main research topics in this study is crystallization and why it should be prevented during LPBF. Despite having already listed numerous advantages of metallic glasses with respect to their mechanical properties, studies have shown that partial crystallization of Zr-based alloys leads to a significant reduction of ductility when compared to the as-cast BMG. That is to say, a decrease in ductility has previously been proven to have been accompanied with an increase in crystallinity. [23] Another study has corroborated that partial crystallization of a Zr-based bulk metallic glass led to a significant increase in fatigue-crack growth rate and caused a marked reduction in the fracture toughness of the BMG. [24] Given that the generation of crystalline phases is largely temperature dependent, it is important to consider the effects of laser-based additive manufacturing on the microstructure of Zr-based BMGs. [25] It is for instance known, that the heat generated by the laser is responsible for creating a heat affected zone (HAZ). The HAZ is typically characterized as a region in close proximity to the melt pool, resulting from partial melting as heat spreads outward from the center of the melt pool to the adjacent powder. [18] Temperature fluctuations will occur every time a new layer is generated, leading to potentially unwanted solidification and melting within and around the HAZ. Hence, this is where parameter optimization is necessary in order to ensure that the heating and cooling of the thermal cycles do not lead to crystallization. [26] Similar to its influence on the relative density of printed parts, the energy density from selective laser melting processes also has a significant effect on crystallization. While keeping all other parameters constant, Figure 3 indicates that the fraction of amorphous content generated is proportional to the scan speed and inversely proportional to the laser power. [27]

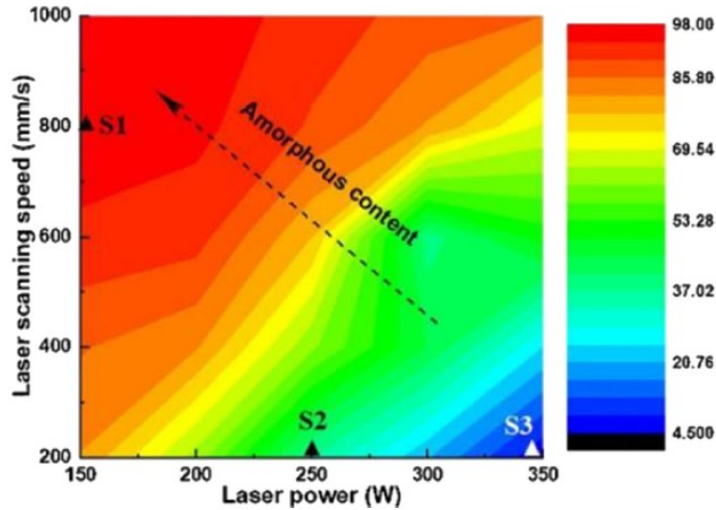


Figure 3: Contour plot highlighting the relationship between laser power, scanning speed and amorphous content for Fe-based BMGs [27]

Figure 4 shows the behavior of a metal as it cools for two distinct cases. When cooling a metallic glass from its liquidus state, a transition to the metastable supercooled liquid state takes place. After a certain amount of undercooling, all crystalline metals will form nuclei and crystallize completely, following pathway (1). If, however, amorphous metals are quenched fast enough in accordance with pathway (2), crystallization can be avoided, which instead leads to the formation of a glassy solid by the time the fictive temperature T_{fic} is reached. [28]

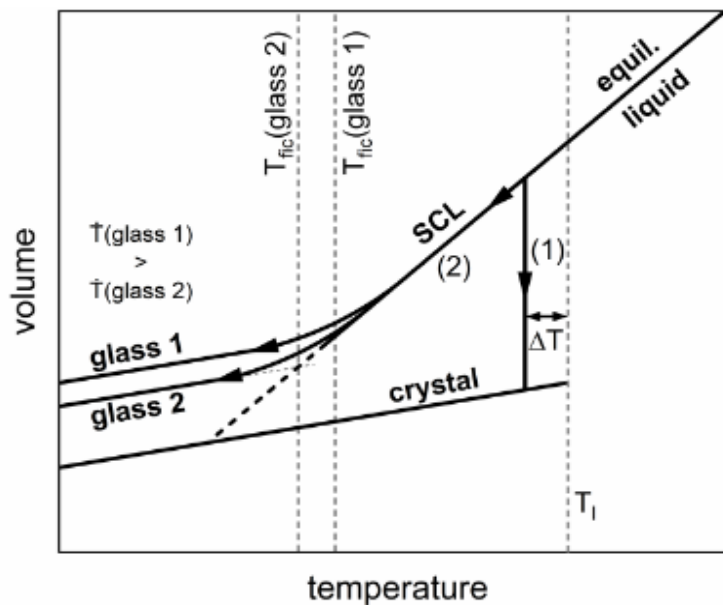


Figure 4: Schematic representation of the volume of a metallic liquid as it cools, as a function of temperature. As the liquid is cooled from its liquidus temperature T_l , it can either crystallize as indicated by pathway (1), or be further undercooled in which a glass is formed after reaching the glass transition temperature T_{fic} . [28]

With regard to AMZ4, an in-depth study of its critical crystallization properties during additive manufacturing was done by Navid Sohrabi. [26] As a result of being highly sensitive to crystallization, the heating and cooling rates of the material during printing are undoubtedly the limiting factors to producing samples of superior quality. Estimated to be approximately 45,000 K/s, the critical heating rate to avoid crystallization is determined to be 18 times the critical cooling rate. These claims are supported by a series of Flash DSC experiments that were conducted using various cooling and heating rates. For example, in order to determine the critical cooling rate, a set of samples were heated at a rate of 5000 K/s after having been previously cooled at different rates from 200 K/s to 40000 K/s. A threshold was then determined in the form of the presence of an exothermic peak, indicating crystallization that had not previously taken place during the cooling cycle. Figure 5 depicts the outcome of this experiment by illustrating the cooling rate as a function of glass transition intensity and crystallization enthalpy. The literature goes on to state that a cooling rate of 10^3 - 10^8 K/s is to be expected within the immediate vicinity of the melt pool when processing AMZ4 via LPBF. [16] The same range can be assumed for the heating rate, with variations being attributed to the process parameters used. Moreover, it is necessary to mention that the crystallization as a result of not reaching the rates mentioned above, is an occurrence that takes place during the thermal cycles experienced at arbitrary points within the sample, with the successive addition of new layers. [26, 16]

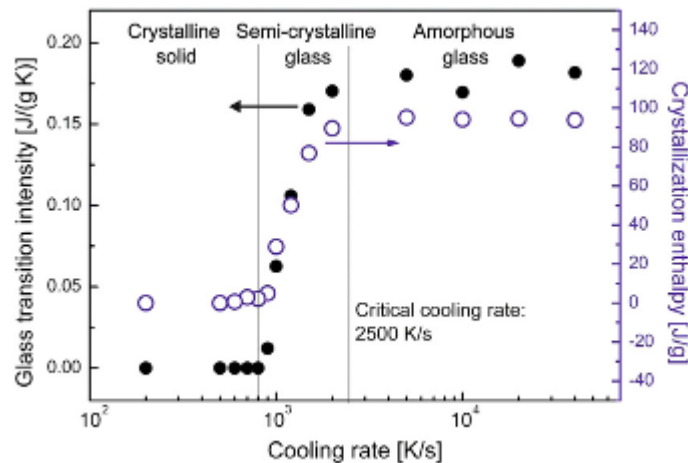


Figure 5: Graphical depiction of the dependence of the glass transition intensity and the crystallization enthalpy on the cooling rate of AMZ4. Three regions are shown to indicate at what cooling rate a crystalline solid, semi-crystalline glass and amorphous glass is formed, respectively. [26]

Although AMZ4 undoubtedly falls under the classification of a BMG, one must be aware of the differences between the characteristics of the powder form and the high purity cast form. A significant concern to many researchers in the field is the fact that the glass-forming ability (GFA) of the powder is much lower than the GFA when cast, largely due to the effect of parameter variation, and thus, temperature fluctuation. [27] It is also possible to qualitatively compare the GFA of the casting process with the GFA of TPF using a time-temperature transformation diagram (TTT) as per Figure 7. In this case, isothermal conditions at temperatures just slightly above T_g permit lower cooling rates than for instance, casting, as well as LPBF. [9] To put the GFA of laser-based additive manufacturing into perspective, one should consider claims made by Zhang et al. He states that although the temperature of the HAZ may be greater than T_g , it has been determined that the window of this high-temperature range, approximately 0.8ms, is indeed very short. In theory, crystallization resulting from nucleation is possible within this time period, however, findings show that in practice, a slightly longer incubation time of 1.87ms is required, due to kinetic factors. It is, however, important to not only evaluate the influence of the manufacturing process, but also the influence of different alloys when considering the crystallization behavior of BMG's. In accordance with Figure 6, the cooling conditions of Zr-based amorphous alloys are presented in the form of another TTT, which, due to the stability of zirconium atoms, happen to be less severe than those of Fe-based metallic glasses. [27] Additionally, in support of previously made claims, the critical heating rate, indicated as R_h , is shown to be far greater than the critical cooling rate R_c .

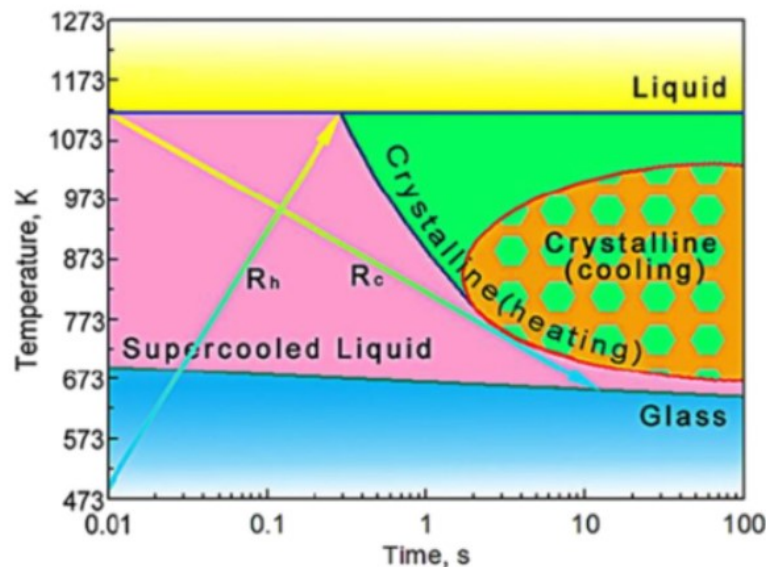


Figure 6: TTT diagram of a Zr-based BMG demonstrating the required critical heating rate R_h and critical cooling rate R_c required to avoid crystallization [27]

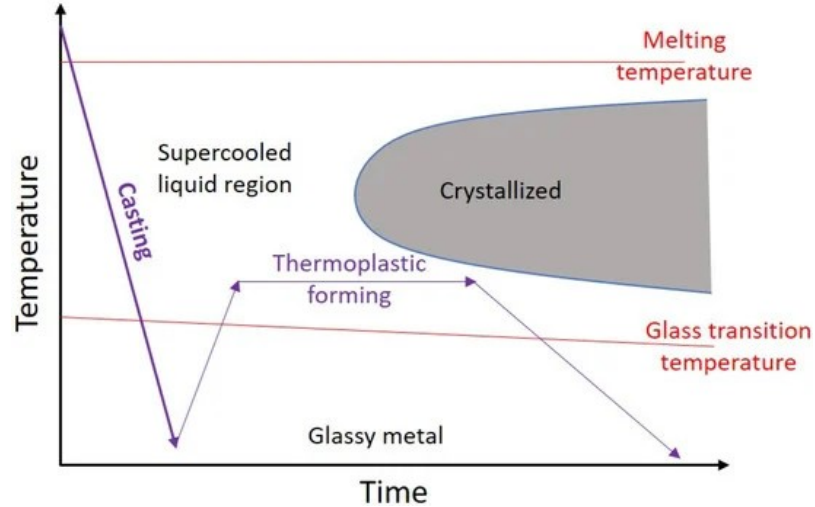


Figure 7: TTT of BMGs showing the cooling kinetics required for casting and thermoplastic forming [9]

3.5 Nucleation and Growth

To gain a better understanding of the phenomenon behind crystallization, the following section aims to provide an insight into classical nucleation theory (CNT). Essentially, nucleation refers to the initial stage of crystal formation when atoms attach to a cluster and form a new, crystalline phase from an existent parent phase, also referred to as a solution. [29] CNT states that the energy difference between the amorphous and crystalline phases during nucleation can be defined in terms of the energy released per atom in a crystalline cluster containing n atoms, in conjunction with the surface energy required to generate the interface. This can be expressed mathematically as follows:

$$\Delta G(n) = n\Delta G' + (36\pi)^{1/3}\bar{v}^{2/3}n^{2/3}\sigma \quad (2)$$

Here, $\Delta G'$ is the difference in Gibbs free energy per atom, \bar{v} is the average atomic volume and σ is the interfacial energy per unit area. [30] For an arbitrary temperature, there exists a critical cluster size n^* , where the change in Gibbs energy reaches a global maximum. It is this point that is considered the energy barrier for nucleation, which corresponds to the activation energy necessary for crystallization to take place. Therefore, any clusters smaller than n^* are likely to dissolve, whereas those greater than n^* will have the tendency to grow. [31]

The importance of treating the temperature independence of nucleation and growth separately was highlighted by Shen et al. in accordance with CNT. [32] This must be done due to the fact that the nucleation rate under rapid heating or cooling is not constant, contrary to previously made assumptions. Therefore, both steady state and transient nucleation must be considered when processing AMZ4. [30] For simplicity however, thermal finite element methods (FEM) used to predict the extent of nucleation in the material, such as the one implemented by Johan Lindwall, may rely solely on the assumption of steady state nucleation. [31] Lindwall uses the Johnson-Mehl-Avrami-Kolgomorov (JMAK) equation in order to predict the amount of crystal fraction formed from an arbitrary thermal history.

$$x = 1 - \exp \left(-k_0 \exp \left(-\frac{E}{RT} \right) t^n \right) \quad (3)$$

Equation (3) is a function of temperature (T) and time (t) whereby k_0 and n are fitting parameters. E is the activation energy, which, along with k_0 and n , were determined from DSC measurements followed by conducting linear regression analysis. [31]

4 Methods and Materials

4.1 Laser Powder Bed Fusion (LPBF)

Laser powder bed fusion technology was utilized in order to print the samples for this study. The model that was used is called MIDI+ manufactured by Aconity, capable of achieving a laser power of up to 400W. Cubic (10mm x 10mm x 10mm), as well as cylindrical samples with diameters of 5mm and heights of 12mm were manufactured with this system. The laser power varied from 33W to 80W, and the scan speed varied from 75mm/s to 710mm/s. The beam diameter was 80 μ m, the hatching distance was determined to be 130 μ m and the layer thickness was chosen to be 30 μ m. It is furthermore also noteworthy to indicate the fact that a bi-directional scanning pattern was used, with a tilt angle between layers of 67°.

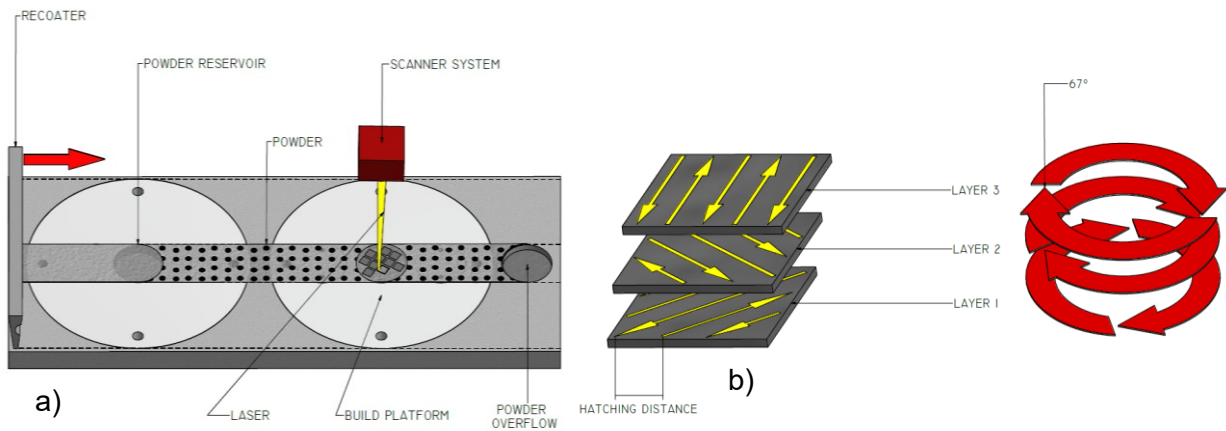


Figure 8: a) Schematic of the Aconity MIDI+ LPBF system with custom fabricated build platform inserts. b) Schematic illustration of the scanning strategy used with a 67° rotation between layers.

4.2 Scanning Electron Microscopy (SEM)

Additively manufactured specimens with rectangular cross sections were embedded in a resin and mechanically polished using a series of SiC papers up to 4000 grit to remove any surface impurities and to obtain a mirror-like finish. They were thereafter polished down to 1 μ m and etched using a solution consisting of 45 mL water + 45 mL HNO₃ + 10 mL HF in order to reveal the microstructure of the samples. [15] The prepared samples were subjected to SEM analysis to study the morphology of the surface and to detect the presence of crystals. The SEM images were taken using a Zeiss Field Emission LEO 1525 scanning electron microscope. The analyses were carried out at a voltage of 20kV and an aperture size of 60 μ m. Images were acquired using the secondary electron detector mode along with the equipped backscattered electron detector to obtain the compositional contrast images of the samples. [33]

4.3 Differential Scanning Calorimetry (DSC)

In order to compare phase transitions across various samples, the Mettler Toledo DSC3+ was used to perform differential scanning calorimetry. First, the samples were prepared by being cut into small pieces weighing approximately 30-50mg. These were placed into aluminum crucibles and sealed with a lid to prevent contamination during the experiment(s). The heating rate was set to 20°C/min and the temperature range was set from 40°C to 700°C. The experiment was carried out under an argon gas flow rate of 50 ml/min. The samples were conditioned at 25°C for 5 minutes before heating. They were then heated from 40°C to 700°C at a rate of 20°C/min while recording the heat flow as a function of temperature. After an isothermal treatment at 700°C, the samples were cooled at a rate of 20°C/min, upon which the heating process was repeated to ensure complete crystallization. The recorded data was analyzed using the instruments built-in software to obtain the glass transition temperature (T_g) and crystallization temperature (T_x) of the metallic glass sample. The enthalpy of crystallization (ΔH_c) was calculated from the exothermic peak observed during the experiment. The results obtained from the analysis were then compared with the powder, and were thereafter used to draw conclusions regarding the optimal process parameters as discussed in the next sections.

4.4 Dynamic Mechanical Analysis (DMA)

Cylindrical samples with a diameter of 5mm and a height of 12mm were manufactured using the abovementioned LPBF method for each set of designated parameters. Smaller samples with rectangular cross sections (1mm x 1.5mm x 10mm) were thereafter extracted from the initial samples using wire electrical discharge machining (EDM). A Discovery HR-3 rheometer from TA Instruments was utilized to conduct a dynamic mechanical analysis on 8 different samples. As a result of the force and displacement limitations of the rheometer, along with the need to generate adequate deflection during testing, 3-point bending was selected as the most suitable load case. A corresponding clamp with a frame length of 8mm was used in order to provide for an overhang of 1mm on each side of the sample(s). With a frequency of 1Hz, a temperature sweep from 30°C to 550°C with a thermal ramp rate of 10°C/minute was conducted. In accordance with the frequency, the samples were subjected to an applied oscillatory force amplitude of 12.5N with a maximum of 25N. In order to aid in temperature control along with preventing oxidation, N₂ was used as a purge gas at a flow rate of 10l/min throughout the duration of the experiments. [34]



Figure 9: 3-point bending DMA experiment test setup showing the deflection of a specimen after the completion of the experiment.

4.5 Semi-Analytical Modeling

4.5.1 State of the Art

Although numerical FEM models may aid in providing accurate information regarding the characteristics of the melt pool, they are time and resource intensive compared to an analytical approach. Therefore, in order to optimize the additively manufactured AMZ4 samples, an analytical model was created with MATLAB, with means to determine the size and temperature of the HAZ. Several critical input parameters were required, including the laser power, scan speed, laser beam diameter, and other significant material properties.

The heat input was calculated analytically using a three-dimensional heat transfer model with a volumetric heat source based on a paper written by P. Zagade. [35] Equation (4) below governs the absorption and conduction of heat energy, where k represents the thermal conductivity, C the heat capacity, T the temperature and ρ the density at a given time t .

$$k \left(\frac{\partial^2 T}{\partial x^2} + \frac{\partial^2 T}{\partial y^2} + \frac{\partial^2 T}{\partial z^2} \right) + \dot{Q} = \rho C \frac{\partial T}{\partial t} \quad (4)$$

In order to ensure a closed-form analytical solution is possible, two significant assumptions must be made. First, one must assume that the boundary conditions considering the solution domain are semi-infinite. Additionally, the heat loss from the top surface due to both radiation and convection must be considered negligible. It is also noteworthy to mention the fact that the beam distribution parameters f_p and f_d , corresponding to the planar and vertical directions, are assumed to both be equal to 3. [36] The amount of energy absorbed by the powder as a function of beam size, distribution of beam energy and depth of the melt pool can then be expressed as:

$$\dot{Q}(x, y, z, t) = \frac{f_p \eta P}{\pi r_b^2} \exp \left\{ -\frac{f_p (x')^2 + f_p (y')^2}{r_b^2} \right\} \times \frac{\sqrt{f_d}}{h\sqrt{\pi}} \exp \left(-\frac{f_d z^2}{h^2} \right) \quad (5)$$

Here, η represents the absorption coefficient of the powder particles, P the laser power, r_b the beam radius, and h the height of the volumetric heat source. The variables x' and y' are linear functions that kinematically describe the position of the laser beam over time. These functions are based on the elapsed time t since the laser beam began traveling from the point (x_s, y_s, z_s) with a constant linear velocity of v_x and v_y in the x and y directions, respectively. Specifically, x' and y' can be described as follows:

$$x' = x - (x_s + v_x t) \quad (6)$$

$$y' = y - (y_s + v_y t) \quad (7)$$

Combining the influence of the boundary conditions with the behavior of the volumetric heat source, Green's function can be implemented to produce Eq. (8), which provides the temperature of a single point with coordinates x , y , and z at a chosen time t .

$$T(x, y, z, t) = \frac{1}{m} \times \left[\left(2m \int_{t'=0}^{t'=t} \frac{2f_p \eta P \sqrt{f_d}}{\rho C_0 \pi \sqrt{\pi}} \frac{1}{\tau''} \exp \left\{ -\frac{f_p \{(x'')^2 + (y'')^2\}}{4f_p \alpha t'' + r_b^2} - \frac{f_d (z'')^2}{4f_d \alpha t'' + h^2} \right\} dt' + (1 + mT_0)^2 \right)^{\frac{1}{2}} - 1 \right] \quad (8)$$

Once again, new parameters are introduced, namely T_0 as the ambient temperature, m and C_0 as material constants, and t'' , x'' , y'' and z'' as variables used for integration purposes as defined in the [35]. One of the concerns with using Eq. (8) is the fact that it only applies to materials that exhibit linear relationships between their temperature T and specific heat C , in the form:

$$C = C_0(1 + mT) \quad (9)$$

4.5.2 Model Implementation

In order to make the model compatible with the glass-forming ability of AMZ4, efforts were made to linearize the nonlinear, piecewise-defined portions of the C_p/T graph for this composition, as shown in Figure 10. [31]

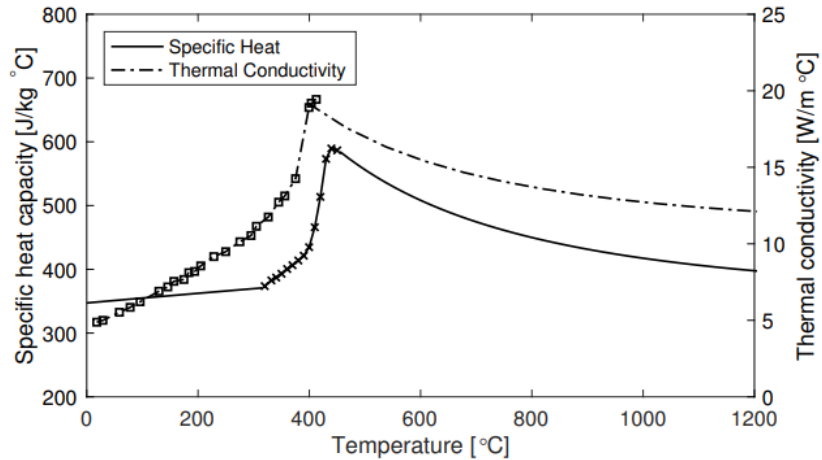


Figure 10: Graphical representation of the change in specific heat capacity and thermal conductivity of AMZ4 with respect to temperature. [37]

Table 1 depicts the temperature boundaries that were chosen for defining the four separate regions. The material constants C_0 and m essentially vary based on an initial temperature output via Eq. (9). The specific heat is then calculated and compared to the value determined from the previous iteration. This process is repeated until the values converge. A detailed derivation of the linear functions used can be found in the appendix.

Table 1: Constants C_0 and m used for the linearization of the specific heat capacity of AMZ4 with respect to predefined temperature ranges.

Temperature Range [°C]	Temperature Range [K]	C_0 [J/kg K]	m [J/kg K ²]
<320	<593	331.71	2×10^{-4}
320-420	593-693	-993.90	-2.31×10^{-3}
420-1200	693-1473	777.69	-3.29×10^{-4}
>1200	>1473	331.71	0.21/T

Using the formulae and boundary conditions defined above, the remaining required material properties of AMZ4, along with the process parameters, were either determined empirically or from readily available literature. Table 2 below provides an overview of these process conditions. Laser power and scan speed(s) were selected in accordance with the chosen print parameters as per Table 3.

Table 2: Material- and process parameters used for the semi-analytical MATLAB model

Parameter	Value	Reference
Laser beam radius, r_b [μm]	40	-
Beam distribution parameters, f_p, f_d [-]	3, 3	[36]
Absorption Coefficient, η [-]	0.35	[28]
Density, ρ [$\text{kg}\cdot\text{m}^{-3}$]	6640	[38]
Ambient temperature, T_{amb} [K]	298	-
Molar gas constant, R [$\text{J}\cdot\text{K}^{-1}\cdot\text{mol}^{-1}$]	8.31	[39]
Solidus temperature, T_s [K]	1150	[40]
Diffusivity, α [m^2/s]	2.1×10^{-6}	[41]
Hatching distance, d_y [μm]	130	-
Layer thickness, H [μm]	30	-

Through the use of the superposition principle, multi-track, multi-layer simulations are also made possible. This is achieved through summing up the heat contributions from all previously printed tracks in addition to the current track. Figure 11a schematically demonstrates the bi-directional scanning path implemented, in which x_s^i and y_s^i denote the starting location of a previously laid i^{th} track and v_x^i and v_y^i denote the corresponding scanning speeds for this track, where start and end times are defined as t_s^i and t_e^i , respectively. The same convention applies to the track being currently scanned, taking into account that the superscript term i is replaced by an f . The distance between two successive tracks, recognized as the hatching distance, is set to $130\mu\text{m}$, equivalent to the setting used during LPBF. Expanding on Eq. (8), the analytical solution for a multi-track simulation becomes:

$$T(x, y, z, t) = \frac{1}{m} \left[\left\{ \frac{4m\eta P f_p \sqrt{f_d}}{\rho c_0 \pi \sqrt{\pi}} \left(\int_{t'=t_s}^{t'=t} \frac{1}{\tau''} \exp \left[-\frac{f_p \{(x_f'')^2 + (y_f'')^2\}}{4f_p \alpha t'' + r_b^2} - \frac{f_d(z)^2}{4f_d \alpha t'' + h^2} \right] dt' + \sum_{i=1}^{i=n_p} \int_{t'=t_s^i}^{t'=t_e^i} \frac{1}{\tau''} \exp \left[-\frac{f_p \{(x_i'')^2 + (y_i'')^2\}}{4f_p \alpha t'' + r_b^2} - \frac{f_d(z)^2}{4f_d \alpha t'' + h^2} \right] dt' \right) + (1 + mT_0)^2 \right\}^{\frac{1}{2}} - 1 \right] \quad (10)$$

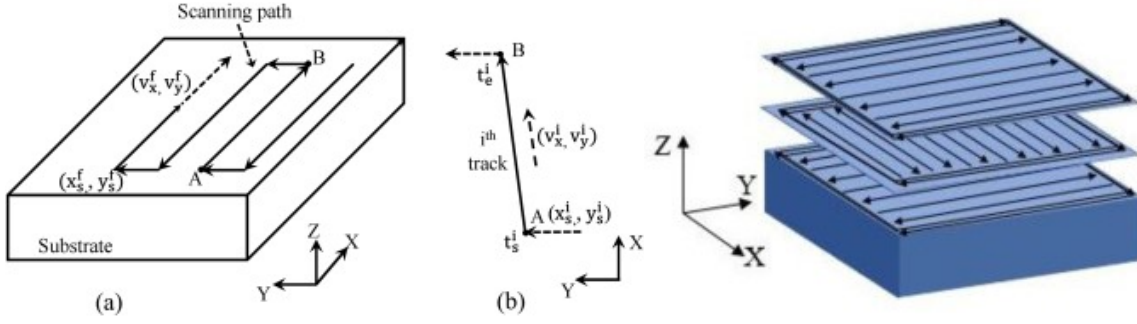


Figure 11: a) Schematic example of a multi-track scanning path as used in the simulations. [35] b) Schematic of the scanning strategy used with respect to layer rotation. [42]

For the purpose of multi-layer modeling, a basic scanning strategy with a hatching angle of 90° between successive layers was utilized. By varying the z coordinate of the point of interest in multiples of the layer thickness ($30\mu\text{m}$) used during printing, the thermal history for any number of layers can be computed.

Despite being able to provide information regarding the thermal history at arbitrary points within the sample, the model is incapable of describing the crystallization kinetics of AMZ4. Therefore, the script was coupled with a function designed to output the degree of crystallization, based on a study by Yang et al. [43] As demonstrated via Eq. (4), the crystal fraction can be determined using the isothermal JMAK model. The inherent limitation of this model is its strict applicability to isothermal phase transformations, which becomes a problem in this study due to the rapidly fluctuating temperatures in the vicinity of the melt pool. Therefore, the non-isothermal Nakamura model is implemented as:

$$X(t) = 1 - \exp \left[1 - \left(\int_0^t K(T) d\tau \right)^n \right] \quad (11)$$

Similar to the JMAK equation, the model is comprised of a temperature dependent rate term $K(T)$, integrated from 0 to time t , along with the Avrami exponent $n = 4$. In order to solve the equation, two key inputs are required, namely the steady-state homogeneous nucleation $I_{ss}(T)$, as well as the growth rate $U(T)$, given by Eq. (12) and Eq. (13), respectively. Moreover, another temperature dependent term $k(T)$ is introduced, related to $K(T)$ as per Eq. (14).

$$I_{ss}(T) = AD_{eff}(T) \exp\left(-\frac{\Delta G^*(T)}{k_B T}\right) \quad (12)$$

$$U(T) = \frac{f}{a_0} D_{eff}(T) \left[1 - \exp\left(-\frac{\Delta G^{l-x}(T)}{RT}\right)\right] \quad (13)$$

$$K(T) = k(T)^{1/n} \quad (14)$$

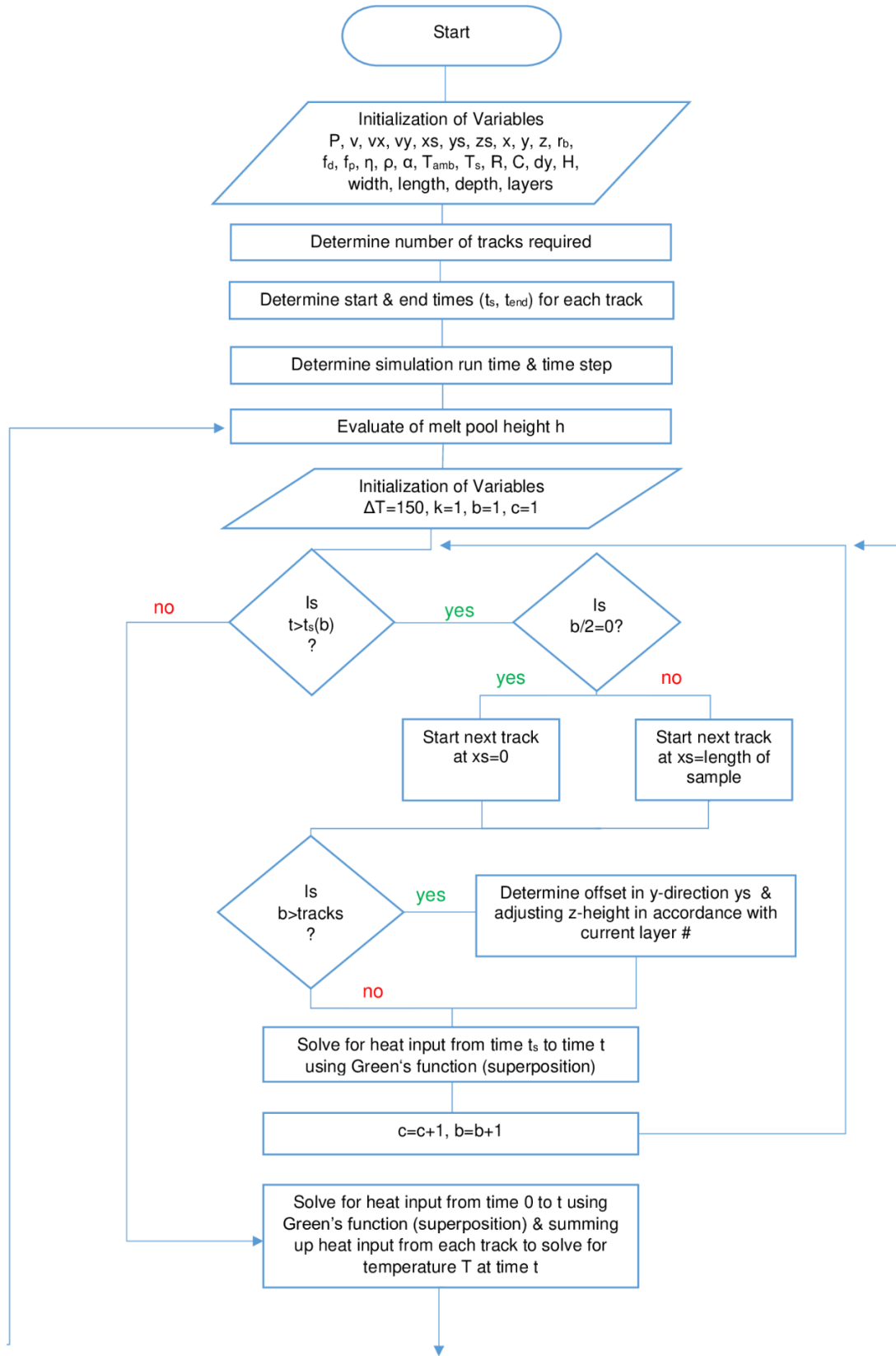
Here, A is defined as the dynamic prefactor, D_{eff} as the effective atomic diffusivity, $\Delta G^*(T)$ as the activation energy, k_b as the Boltzmann constant, f as the interface roughness, a_0 as the average diameter of the diffusing atoms and ΔG^{l-x} as the difference in free energy between the liquid and crystalline phases. Furthermore, due to AMZ4's sensitivity to exposure to oxygen during manufacturing, it is necessary to state that A is based on an oxygen content of 2202ppm. From here, $k(T)$ can be derived as follows:

$$k(T) = \frac{\pi}{3} I_{ss}(T) U(T)^3 \quad (15)$$

Additional assumptions are made in the model. Firstly, it is assumed that the powder is initially entirely amorphous, indicated by $X(0)=0$. Secondly, the thermal bounds of integration are set between 800K and 1203K, where the upper limit defines the liquidus temperature of the alloy. Put simply, the degree of crystallization is reset to zero if the calculated temperature exceeds the melting temperature. For a summarization of the material parameters used to solve Equations (11) - (15) including an explanation of the derivation process, please see [41].

To ensure numeric stability as well as accuracy, it is vital to choose an appropriate time step Δt for the simulation. Given that the forward Euler method is used to solve Eq. (11), a relatively fine time step is typically required. For this reason, various time steps ranging from 1×10^{-3} s- 1×10^{-5} s were experimented with. The conclusion was drawn that anything finer than $\Delta t = 1 \times 10^{-4}$ s resulted in insignificant changes in the results. Therefore, in order to reduce computation times and for simplicity, a fixed time step of $\Delta t = 1 \times 10^{-4}$ s was utilized.

For clarity, a flowchart designed to provide a diagrammatic representation of the logic used in the semi-analytical model is given in Figure 12. The flowchart applies to a multi-track modeling scenario and can therefore be simplified for single-track calculations. As indicated through the use of corresponding predefined process blocks, two functions are called, namely the aforementioned Nakamura function, as well as a “plotcube” function used to generate a visual representation of the solution domain as shown in Figure 21.



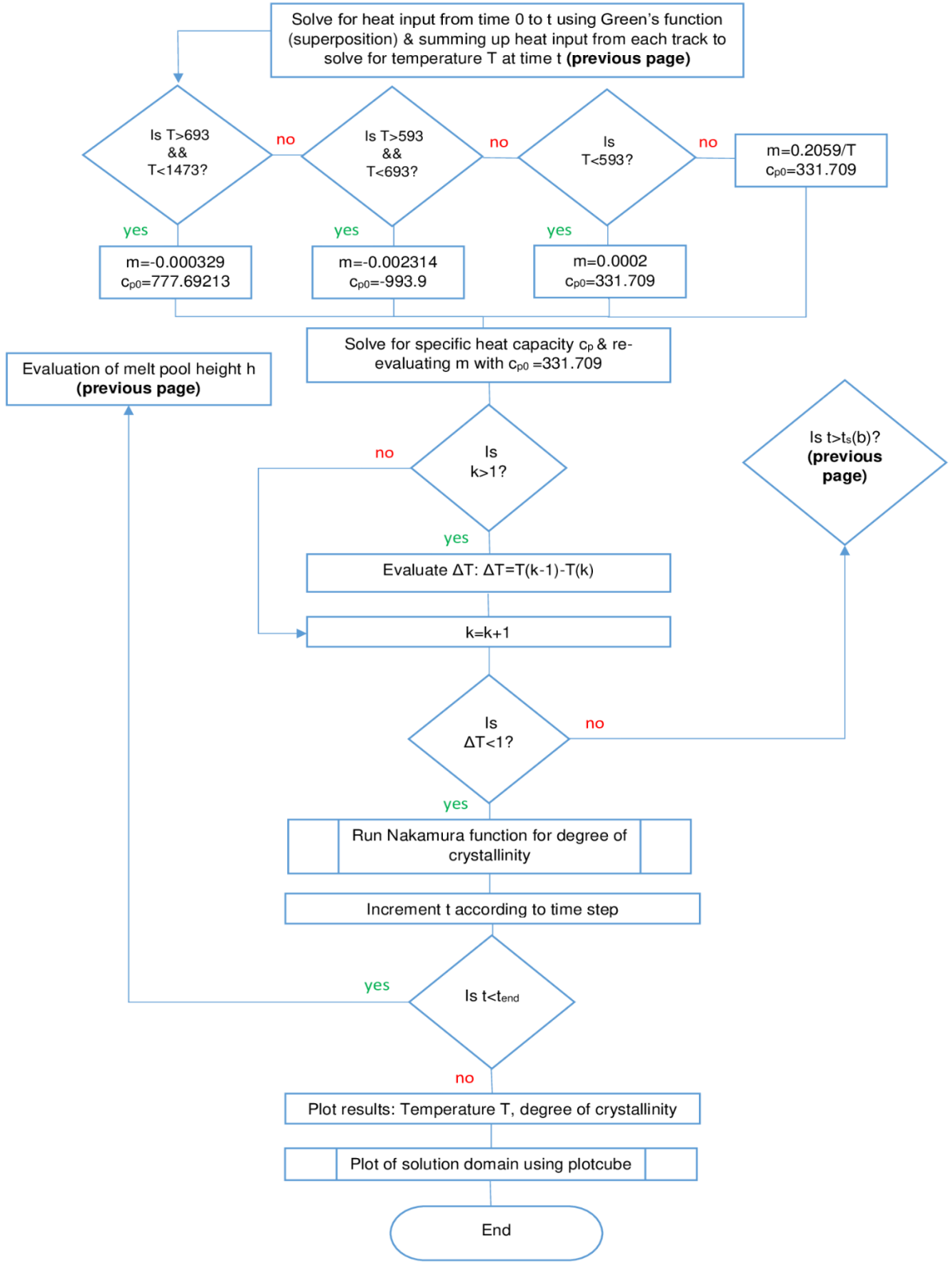


Figure 12: Flowchart for the methodology used in the multi-track, semi-analytically modelled simulations.

5 Results

5.1 Parameter Selection Study

Choosing appropriate parameters for the additive manufacturing of the Zr-based alloy is of utmost importance when it comes to generating baselines for optimization. From literature by Niyou Wang et al., the claim is made that higher energy densities lead to higher crystallization volumes. [44] Consequently however, one must not neglect the need to maintain a high relative density, which increases with increasing laser power and decreasing scan speed. [45] Due to the negative correlation between amorphous content and density of the sample, the energy density must be chosen carefully.

Table 4 lists all sets of samples that were initially printed via LPBF in accordance with the utilized energy densities as a function of laser power and scan speed. The layer thicknesses and hatching distances were held constant at 30 μ m and 130 μ m respectively for all trials. Optical microscopy (OM) was then used to determine the relative density at various points within the sample(s). For the sake of repeatability and reproducibility, three measurements were made per sample at different locations. The mean of each data set was thereafter calculated and can be found in the fourth column of Table 4. Due to an inherent lack of fusion resulting from an insufficient energy density, several relative density values as indicated by asterisks were deemed to be statistical outliers and were therefore excluded from Figure 13 to avoid skewing the trend. The results show, as illustrated in Figure 13, that the samples with the highest relative densities tend to have been manufactured with higher energy densities. More specifically, the logarithmic trend line estimates a relative density of around 99.75% at an energy density of 20J/mm³, which begins to climb before asymptotically approaching a relative density of 100%. The standard error of the sample mean was also calculated, ranging from 1.66 x 10⁻³ - 0.07%, as indicated by the error bars. As a preliminary optimization measure, only the 10 samples processed via parameters yielding porosities of less than 0.1% were selected for further analysis. These are listed in Table 3, in which the types of analyses carried out for each sample are also clearly indicated.

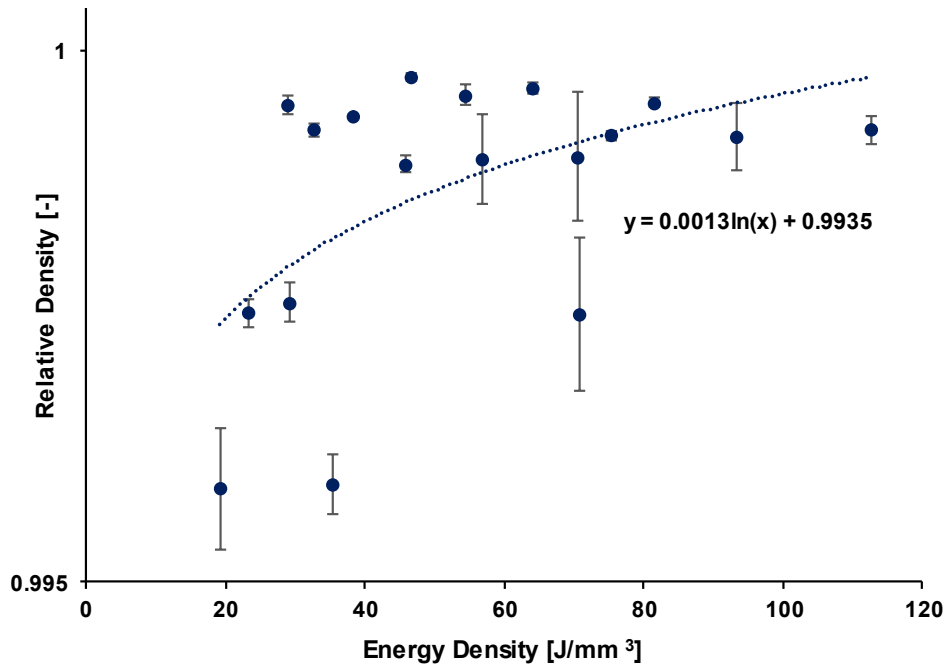


Figure 13: Relationship between relative density and energy density used as criteria for the preliminary parameter selection study.

Table 3: Overview of the analyses conducted for the 10 samples with porosities of less than 0.1%

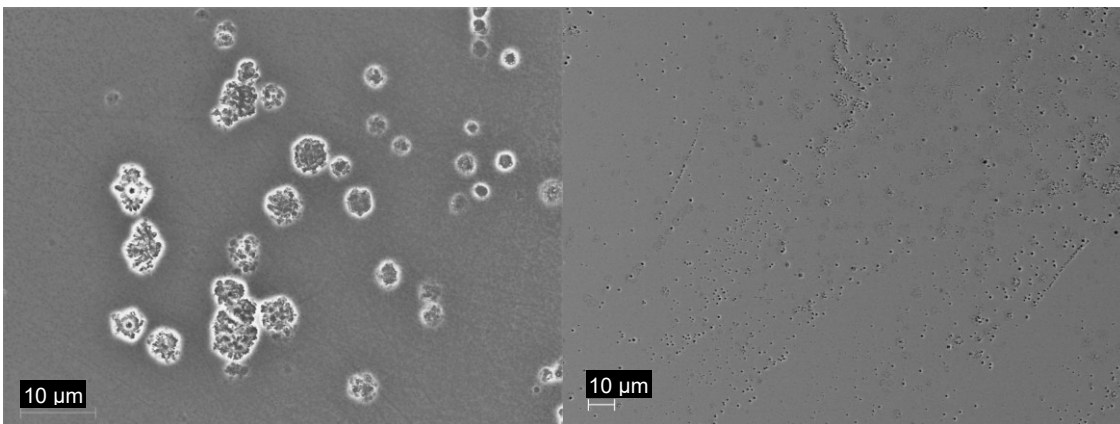
Laser Power [W]	Scan Speed [mm/s]	Energy Density [J/mm ³]	DSC	DMA	SEM	Simulation
33	75	112.82	x	x	x	x
40	110	93.24	x	x	x	x
50	170	75.41	x	x	x	x
60	240	64.10	x	x	x	x
60	400	38.46	x	x	x	x
70	220	81.59				x
70	330	54.39		x	x	x
70	550	32.63			x	x
80	440	46.62	x	x	x	x
80	710	28.89	x	x	x	x

Table 4: Overview of all printed samples with varying energy density initially considered for the parameter selection analysis.

Laser Power [W]	Scan Speed [mm/s]	Energy Density [J/mm ³]	Relative Density [%]	Standard Error [%]
33	75	112.82	99.93	0.01
33	120	70.51	99.90	0.06
33	240	35.26	99.59	0.03
33	650	13.02	95.79*	-
40	110	93.24	99.92	0.03
40	180	56.98	99.86	0.03
40	350	29.30	99.76	0.02
40	1000	10.26	90.14*	-
50	170	75.41	99.92	4.15 x 10 ⁻³
50	280	45.79	99.89	7.78 x 10 ⁻³
50	550	23.31	99.75	0.01
50	1500	8.55	85.13*	-
60	240	64.10	99.96	5.44 x 10 ⁻³
60	400	38.46	99.94	1.66 x 10 ⁻³
60	800	19.23	99.60	0.06
60	2300	6.69	84.98*	-
70	220	81.59	99.95	4.12 x 10 ⁻³
70	330	54.39	99.96	9.27 x 10 ⁻³
70	550	32.63	99.93	5.73 x 10 ⁻³
70	1100	16.32	98.88*	-
70	3000	5.98	86.38*	-
80	290	70.73	99.77	0.07
80	440	46.62	99.98	3.83 x 10 ⁻³
80	710	28.89	99.95	8.65 x 10 ⁻³

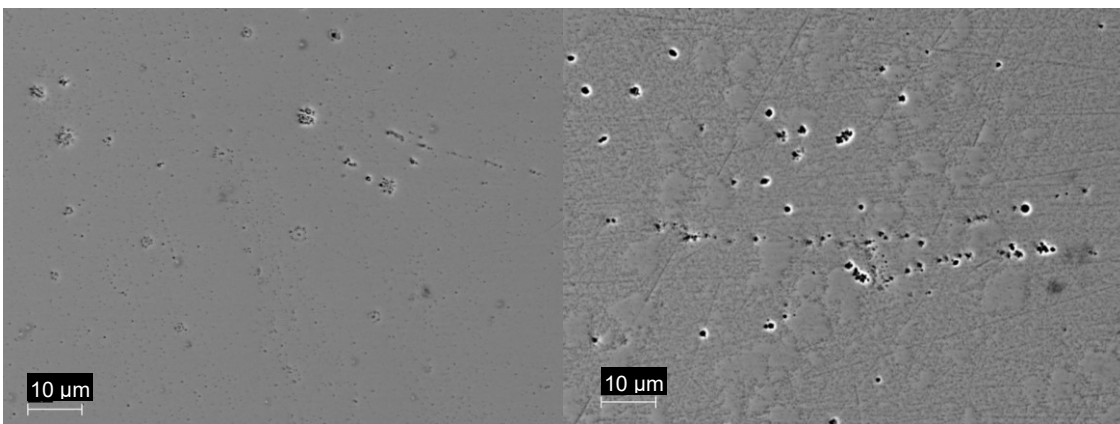
5.2 SEM

Figure 14a) – i) qualitatively depict the crystalline content of additively manufactured AMZ4 for nine different printing parameters. Given that all images were taken with approximately the same level of magnification, it is possible to conclude that a laser power of 70W with a scanning speed of 330mm/s resulted in the greatest amount of crystals along with the largest cluster sizes. Moreover, Figure 14 g) – i) indicate a very scarce presence of crystals when compared to the rest of the samples. Despite these findings, sources of error such as the presence of scratches, contamination, pores and human error during operation of the machine must be considered when analyzing the results.



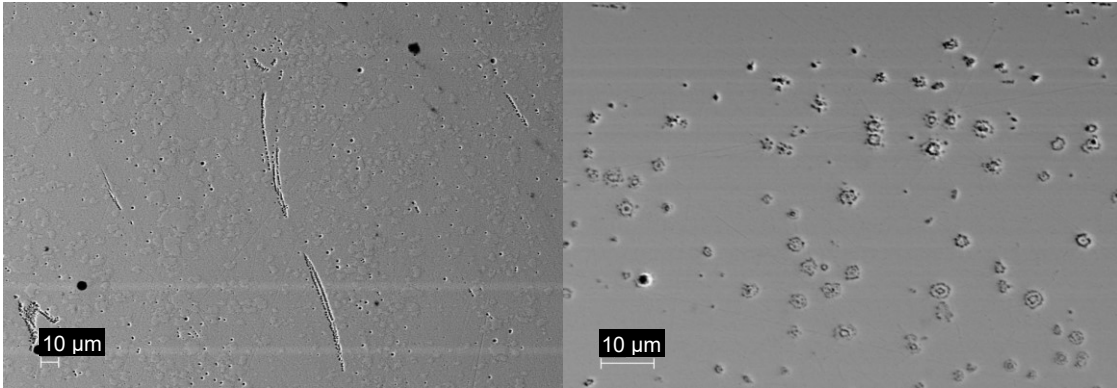
a)

b)



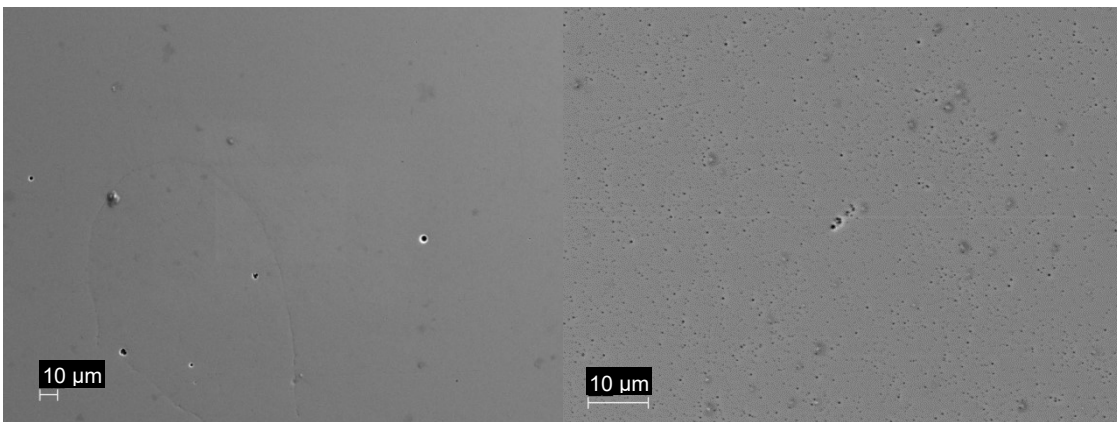
c)

d)



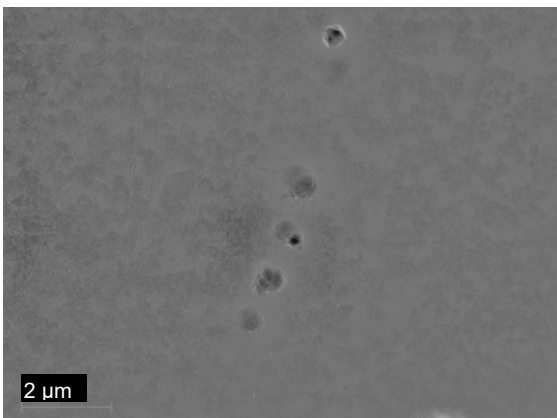
e)

f)



g)

h)



i)

Figure 14: SEM micrographs of samples with varying energy densities obtained via SEM analysis. a) $P=70W$, $v=330mm/s$, b) $P=33W$, $v=75mm/s$, c) $P=80W$, $v=440mm/s$, d) $40W$, $v=110mm/s$, e) $P=50W$, $v=170mm/s$, f) $P=60W$, $v=240mm/s$, g) $P=60W$, $v=400mm/s$, h) $P=80W$, $v=710mm/s$, i) $P=70W$, $v=550m/s$

5.3 LPBF Simulation

Through implementation of the single-track model, it was possible to generate plots depicting the temperature with respect to time at an arbitrary point along the track for all 10 samples in accordance with Table 3. Peak temperatures between 7000 and 9000°C were computed across all sets of parameters. The model was furthermore used to determine the heating and cooling rates within the first 5-10 milliseconds of the simulation as the laser passes over the point of interest. The heating rates varied from 2.87×10^6 - 3.5×10^6 °C/s whereas the cooling rates ranged from 9.48×10^5 - 2.84×10^6 °C/s. As a result of the non-linear relationship between temperature and specific heat, a significant decrease in the cooling rate was observed after the glass transition temperature was reached. Figure 16 illustrates the behavior of the heating and cooling rates with respect to energy density. As such, a noticeable increase in the heating rate is observed with increasing energy density, until reaching a maximum at around 75 J/mm³. The heating rate then decreases further, mimicking the characteristic of a quadratic function. As such, a second-degree polynomial regression model was used to describe the trend. The same cannot be said when analyzing the cooling rates, where an exponential decay is witnessed as the energy density increases. In summation, it can be concluded that, according to the results of the simulation, decreasing laser power and increasing scan speed lead to longer cooling times, whereas increasing laser power and decreasing scan speeds lead to higher heating rates up to a threshold of 75 J/mm³.

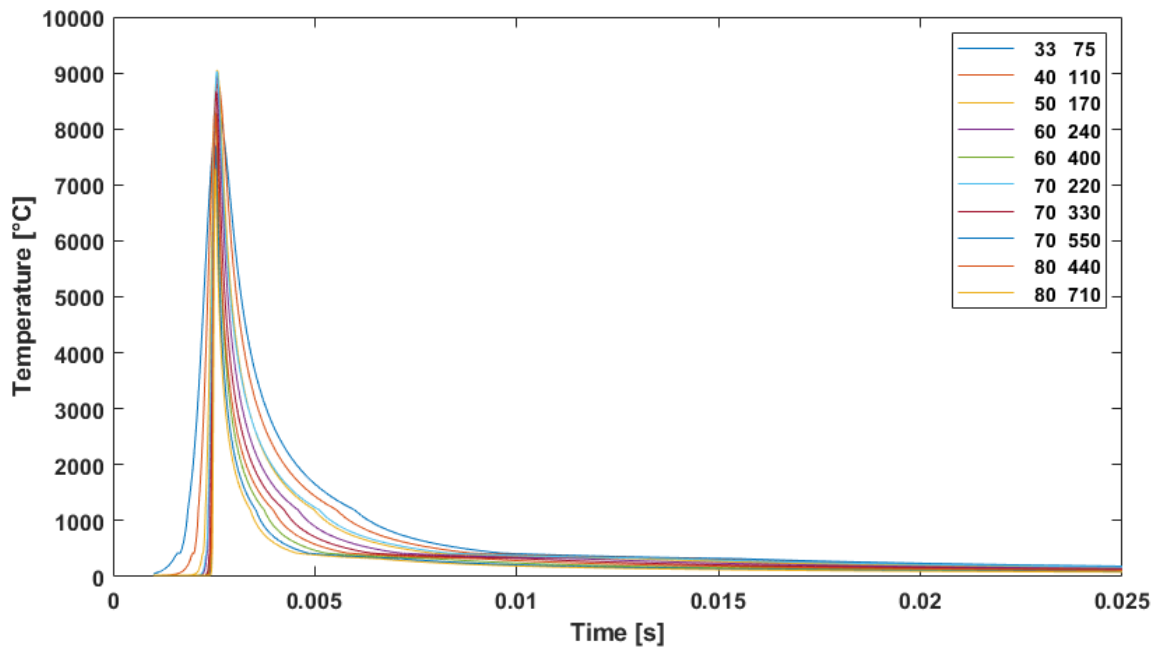


Figure 15: Thermal history of 10 samples with varying energy densities from single-track simulations.

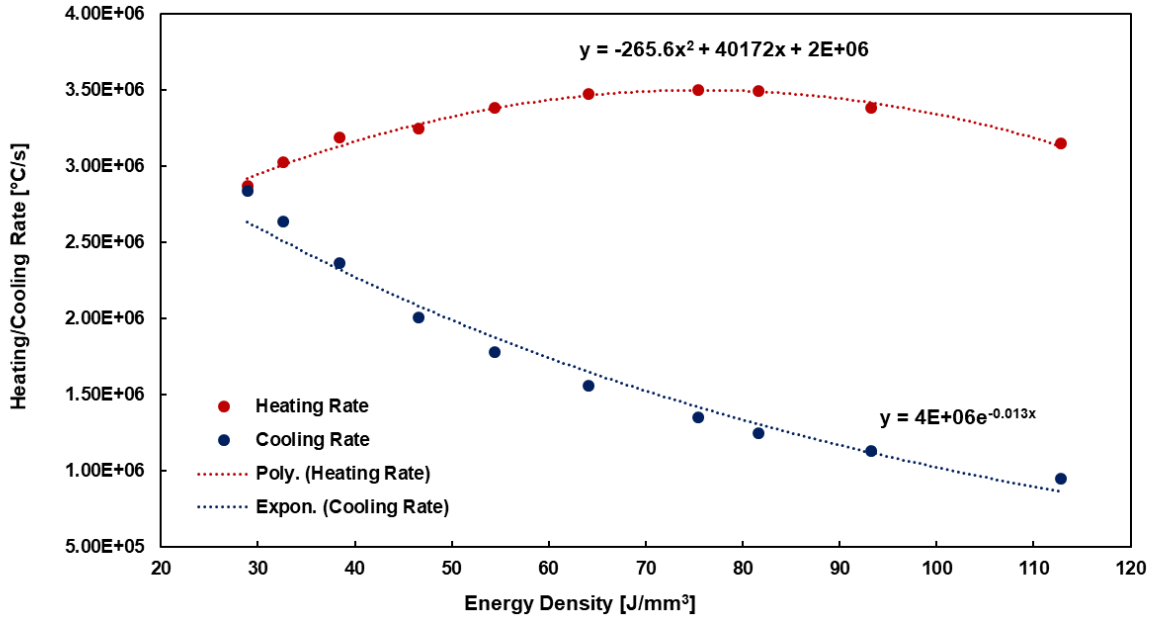


Figure 16: Heating and cooling rates as a function of energy density when the laser passes over the point of interest during single-track simulations.

In addition to the single-track simulation, a multi-track, multi-layer model was also created, enabling the ability to gain a deeper understanding of the thermal history, as well as the crystallization kinetics during the LPBF manufacturing process of Zr-based BMG samples. The temperature over time for the fabrication of 11 layers of a 5mm x 5mm sample with a laser power of 70W and a scanning speed of 220mm/s is given by Figure 17, where each layer takes about 0.9s to complete. The point being evaluated is located in the center of the sample, as illustrated in Figure 21. Furthermore, the reason for simulating the printing of precisely 11 layers lies in the fact that the increase in crystallinity beyond this depth can be considered negligible. A maximum temperature of 5254°C is observed during the scanning of the first layer, as the laser approaches the center of the sample. After the completion of each subsequent layer, this central peak becomes gradually less prominent, decreasing in temperature, and reaching a minimum of 544°C on layer 11. Using the Nakamura model, the degree of crystallinity was also determined as shown in Figure 18. Based on the assumption that the powder is initially entirely amorphous, the conclusion can be drawn that nucleation really only begins to take place as a result of reheating caused by the heat generated from the printing of the sixth layer, as indicated in Figure 18 at a time of around 5s. From this point on however, the crystal fraction increases significantly with the addition of each layer, although the largest increase occurs during processing of the seventh layer, where a growth from 0.28% to 4.91% is observed. Eventually, by the end of the 10.8s simulation, the crystal fraction growth approaches 0, leading to a degree of crystallinity of 10.82% once the final (11th) layer is processed. For comparison's sake, the maximum crystalline fraction of all other

manufactured samples is depicted in Table 5. It is therefore evident that an energy density of 28.89J/mm^3 results in the lowest crystalline fraction of $6.9 \times 10^{-6} \%$, whereas an energy density of 81.59J/mm^3 results in the highest obtained crystalline fraction of 10.83% , 11 layers down from the top of the sample. Despite observing a positive trend, the findings appear to reinforce the fact that the crystallization kinetics of AMZ4 do not entirely depend on the energy density, contrary to what is often stated in the literature. [45] Furthermore, the duration of the respective crystallization processes for all evaluated samples is given in Figure 20. At lower energy densities, the onset of crystallization takes place during printing of layer 3, whereas the endset takes place between layers 4-5. As the energy density increases, a positive trend is observed, in which the window of crystallization, which varies from 1-5 layers, moves to deeper layers within the sample(s).

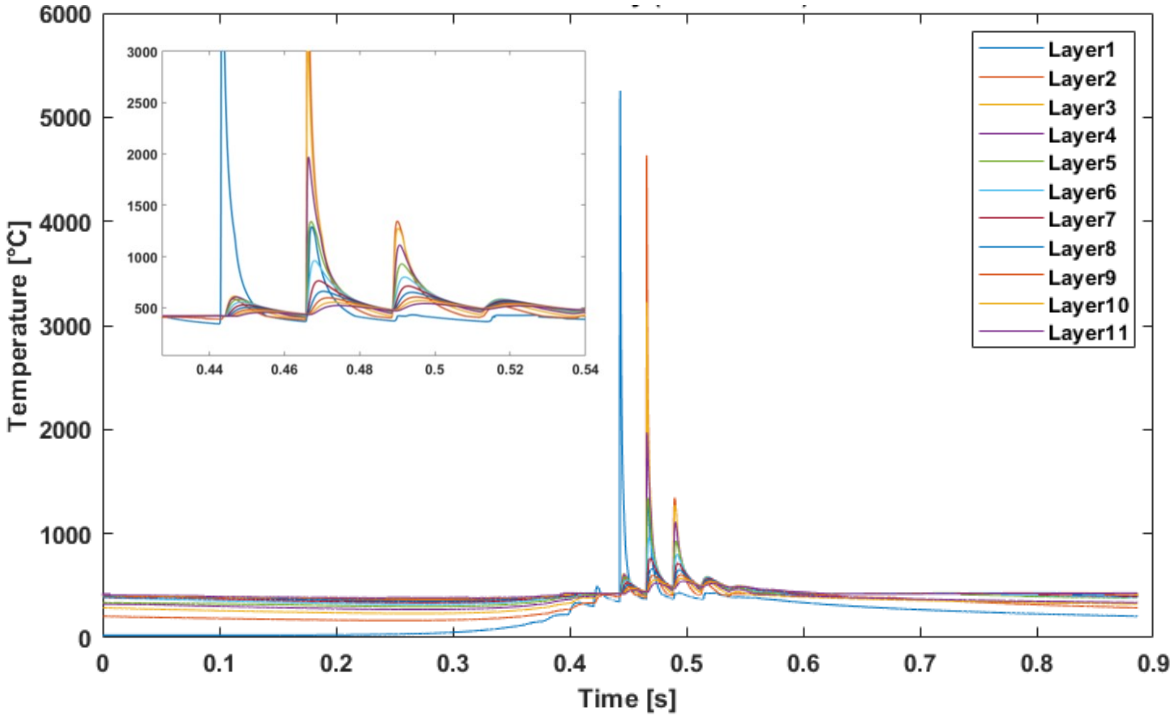


Figure 17: Thermal history of an 11 layer, multi-track simulation of a sample printed with a laser power of 70W and scanning speed of 220mm/s.

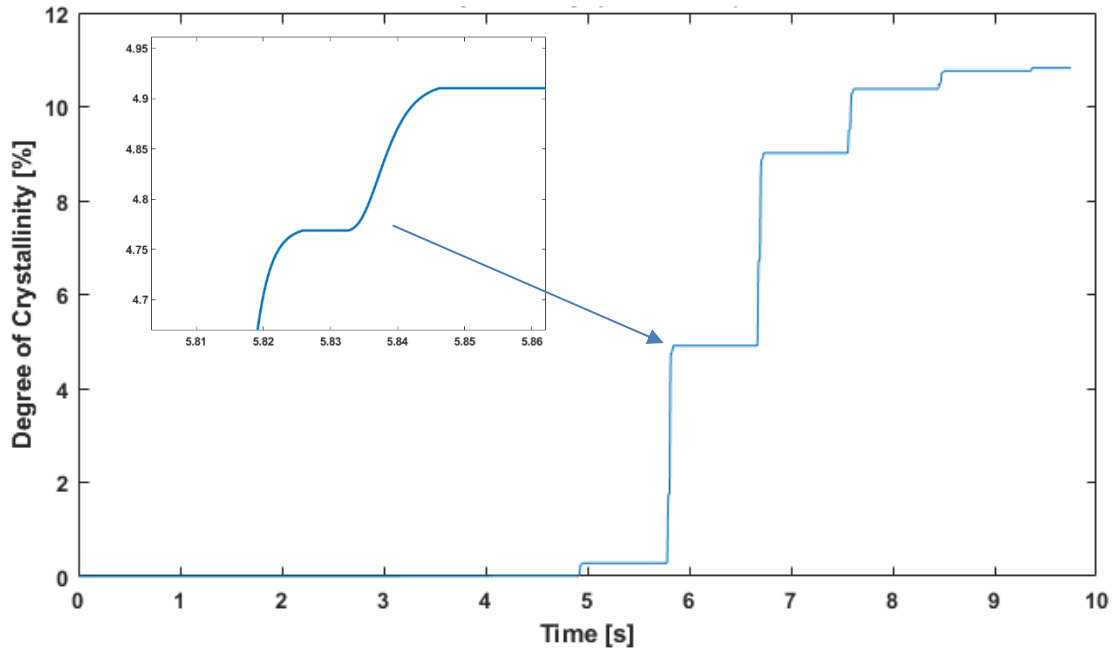


Figure 18: Degree of crystallinity resulting from an 11 layer, multi-track simulation of a sample manufactured with a laser power of 70W and a scanning speed of 220mm/s (corresponding to an energy density of 81.59J/mm³). The crystallinity is predicted at a point in the middle of the sample, at a depth of 11 layers from the surface.

Table 5: Predicted degree of crystallinity in accordance with the results from Figure 19.

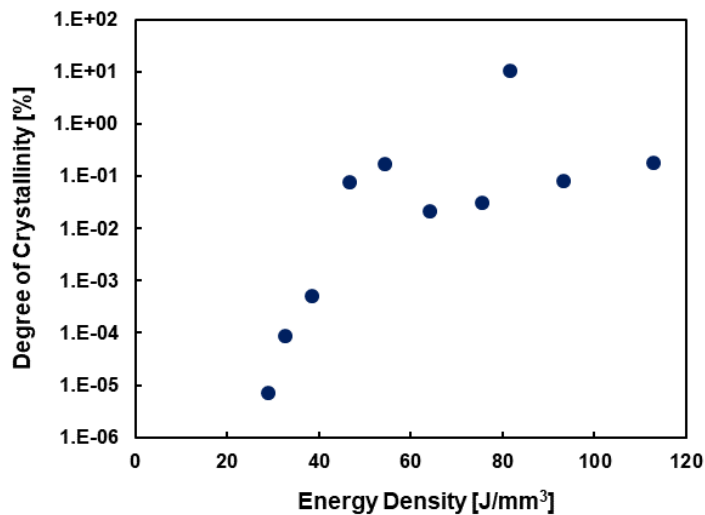


Figure 19: Predicted degree of crystallinity as a function of energy density for 10 different samples. The duration of each multi-track, multi-layer simulation spans 11 layers.

Energy Density [J/mm ³]	Degree of Crystallinity [%]
28.89	6.9 x 10 ⁻⁶
32.63	8.8 x 10 ⁻⁵
38.46	5 x 10 ⁻⁴
46.62	0.08
54.39	0.18
64.10	0.02
75.41	0.03
81.59	10.83
93.24	0.08
112.82	0.19

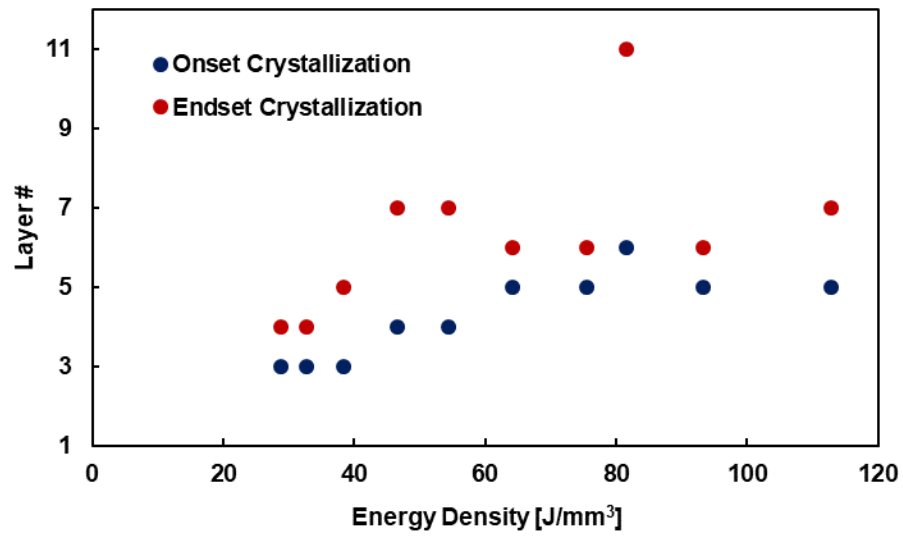


Figure 20: Onset and endset of crystallization as a function of energy density during multi-track simulations.

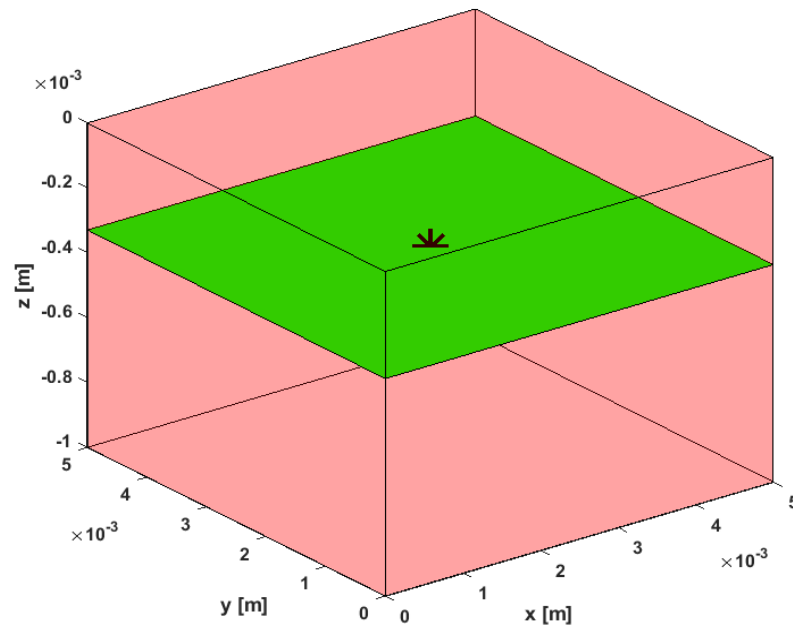


Figure 21: Location of the solution domain for determining the degree of crystallinity of a 5mm x 5mm sample pertaining to all multi-track simulations.

5.4 DSC

A series of seven DSC measurements were carried out in accordance with the method highlighted in the previous section. With reference to Figure 22, the first two digits of each curve name denote the laser power in watts and the following digits define the scanning speed in mm/s. As the material is heated at a constant heating rate, the samples experience relaxation followed by glass transformation at approximately 400°C, characterized by a baseline shift. A distinct exothermic event takes place at around 460°C, indicative of an assumed crystallization process representing the latent heat of transformation. [46] The behavior of all samples is highly similar, with only minor quantifiable variations that can be observed and measured.

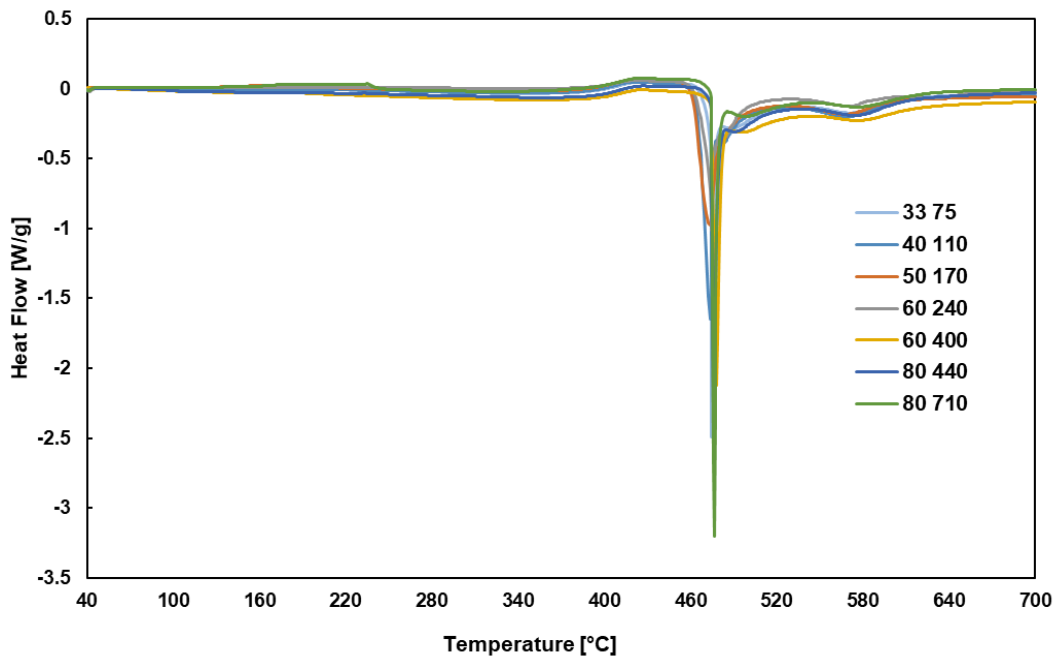


Figure 22: DSC curves of all samples investigated when heating from 40°C – 700°C at a heating rate of 20°C/min

Table 6: Overview of the DSC results for all samples investigated

Energy Density [J/mm ³]	T _g Onset [°C]	T _x Onset [°C]	ΔT _x [°C]	Relaxation Enthalpy [J/g]	Crystallization Enthalpy [J/g]
112.82	396 ± 1	472 ± 1	75 ± 1	-4.02 ± 0.05	-27.70 ± 0.05
93.24	394 ± 1	466 ± 1	72 ± 1	-4.32 ± 0.05	-23.07 ± 0.05
75.41	393 ± 1	463 ± 1	69 ± 1	-4.78 ± 0.05	-21.61 ± 0.05
64.10	396 ± 1	466 ± 1	71 ± 1	-2.84 ± 0.05	-14.89 ± 0.05
46.62	398 ± 1	474 ± 1	77 ± 1	-3.12 ± 0.05	-27.22 ± 0.05
38.46	399 ± 1	475 ± 1	76 ± 1	-3.68 ± 0.05	-28.05 ± 0.05
28.89	398 ± 1	475 ± 1	77 ± 1	-5.16 ± 0.05	-31.28 ± 0.05

Upon further analysis, various parameters were evaluated including the onset of glass transition T_g, the onset of crystallization T_x, the relaxation enthalpy and the crystallization enthalpy. The respective values are listed in Table 6 as a function of energy density. To account for experimental errors, an uncertainty of ±1°C was assigned to T_g, T_x, and ΔT_x measurements, while an uncertainty of ±0.05J/g was assigned to measurements of relaxation and crystallization enthalpy. The results indicate that the values of T_g^{onset}, as well as T_x^{onset} decrease with increasing energy density, but only up till approximately 75J/mm³, after which a positive correlation is apparent. Thus, these findings do not fully agree with a study conducted by Marattukalam et al., in which a strict positive correlation between the above-mentioned variables was observed. [38] Subtracting the onset of crystallization from the onset of glass transition provides the supercooled liquid range ΔT_x, which is essentially an indirect measure of the GFA. [47] Figure 24 shows the dependency of the experimentally observed ΔT_x on energy density, where a quadratic trend line proves to best resemble the relationship between the variables. Based on the obtained results, the GFA also approaches a minimum at or around 75J/mm³. In regard to the relaxation and crystallization enthalpies, Figure 25 illustrates once again the dependence on energy density. Upon analyzing the data, it becomes apparent that for most samples, no significant trend between the recorded enthalpies and the process parameters was witnessed. It is however, important to note that the sample processed with an energy density of 64.10J/mm³ exhibits the lowest enthalpy during both relaxation and crystallization phases.

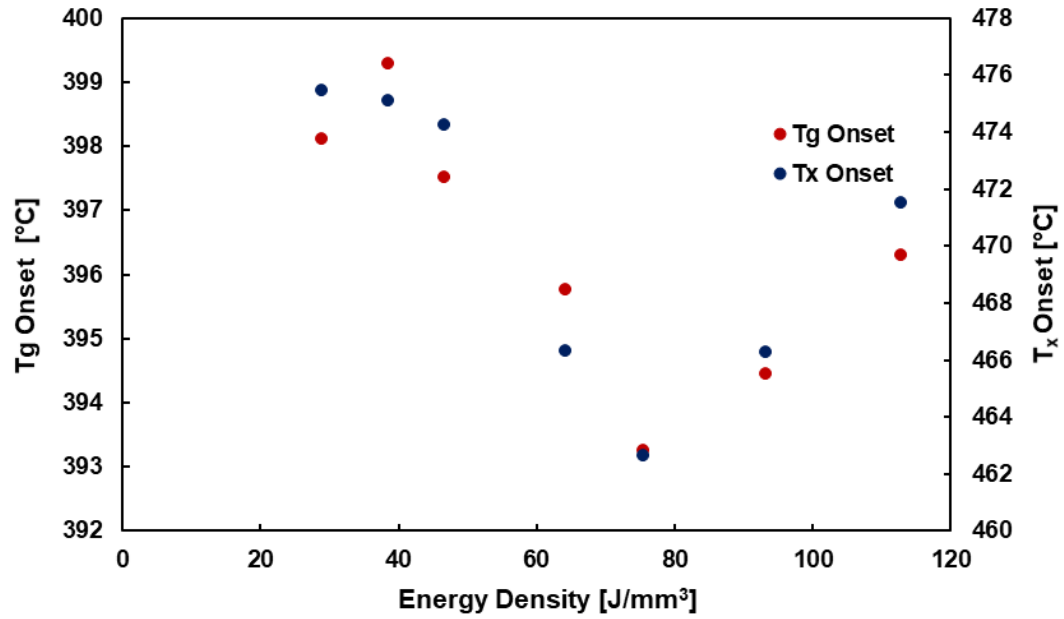


Figure 23: Onset of glass transition T_g and crystallization T_x with respect to energy density according to DSC results.

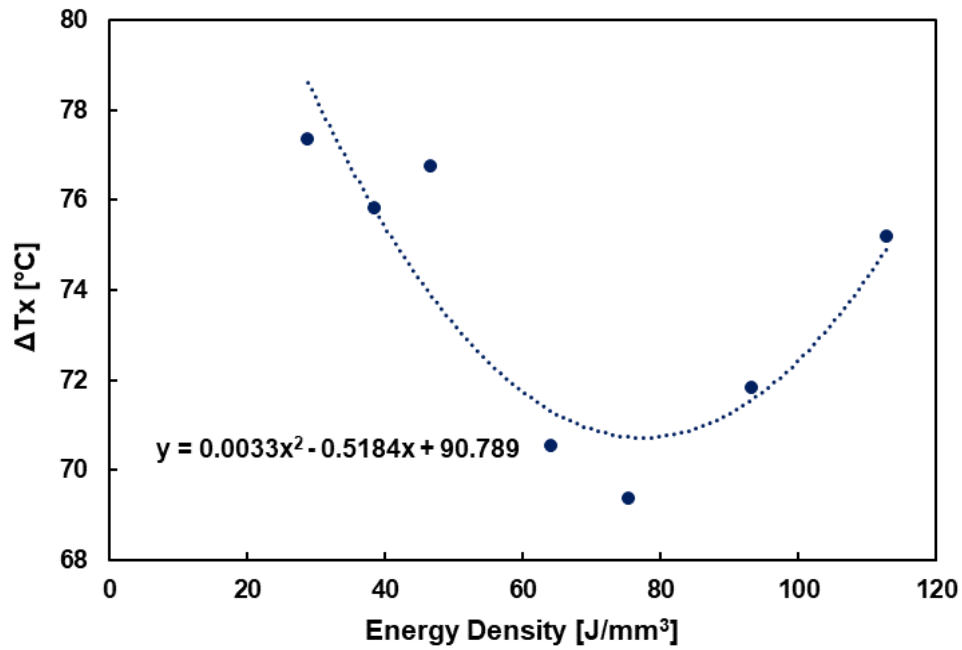


Figure 24: Glass-forming ability ΔT_x (recognized as the difference in temperature between the onset of crystallization T_x and the onset of glass transition T_g) with respect to energy density

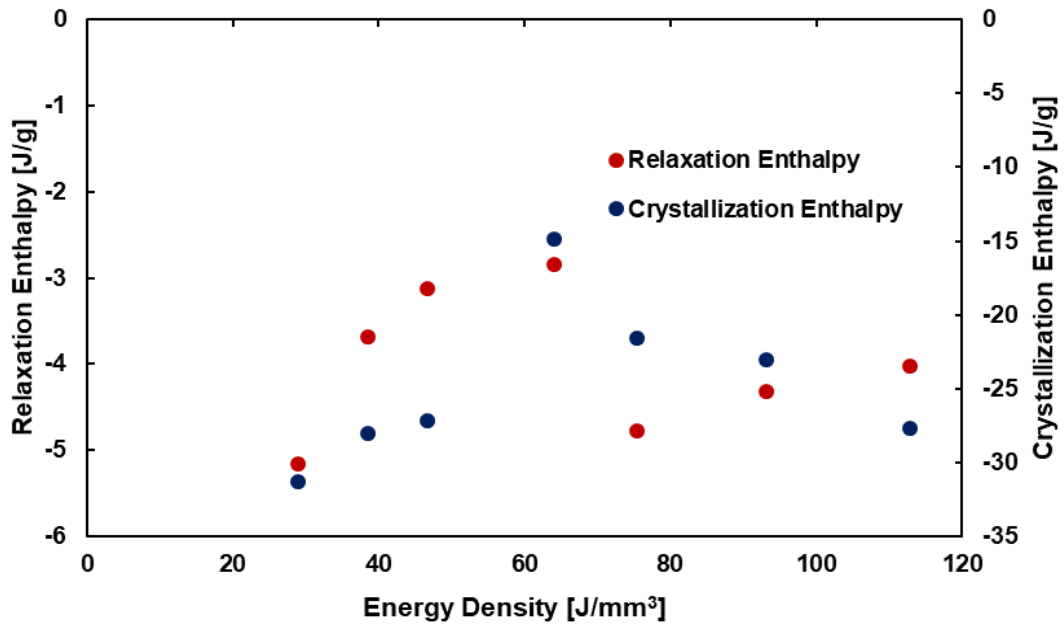


Figure 25: Relaxation enthalpy and crystallization enthalpy with respect to energy density according to DSC results.

5.5 DMA

Similar to Young's Modulus, the storage modulus (E') is a measure of the energy stored, whereas the loss modulus (E'') characterizes the energy dissipated by the material. [48] Both of these parameters, in addition to the ratio of the loss to the storage as denoted by $\tan \delta$, were evaluated after performing a series of DMA analyses, with means to further characterize the samples in regard to their stiffness and damping properties. This is shown logarithmically in Figure 26 for a sample manufactured with a laser power of 33W and a scanning speed of 75mm/s. It is evident that as the temperature approaches the aforementioned experimentally determined glass transition temperature, the storage modulus decreases, resulting in an increase of the loss modulus. This in turn, consequently, causes the damping factor $\tan \delta$ to rise, indicative of a softening of the material. Prior to the onset of glass transformation at approximately 400°C, the value reaches a maximum across all samples, within the range of 0.1-0.12. Efforts to better understand the relaxation characteristics of the material were also made as illustrated in Figure 27, where $\tan \delta$ is plotted against the temperature, from 200-400°C. All samples appear to behave similarly up until about 280°C where a distinct shoulder is observed, after which the curves begin to diverge from one another. After conducting qualitative analysis, it can be concluded that the sample produced using a laser power of 70W and a scanning speed of 330mm/s exhibits the greatest thermal stability. Conversely, the combination of a laser power of 60W and a scanning speed of 240mm/s results in the lowest thermal stability. In other words, these specific parameters yield the lowest and highest mean $\tan \delta$ values respectively, within the temperature range defined above.

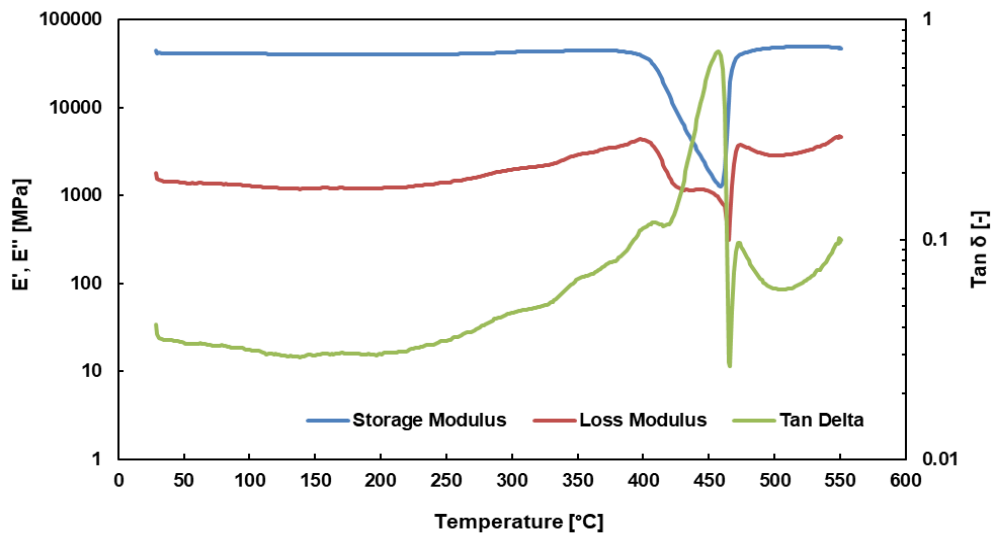


Figure 26: DMA results depicting E' , E'' $\tan \delta$ as a function of temperature of a sample manufactured with a laser power of 33W and a scanning speed of 75mm/s.

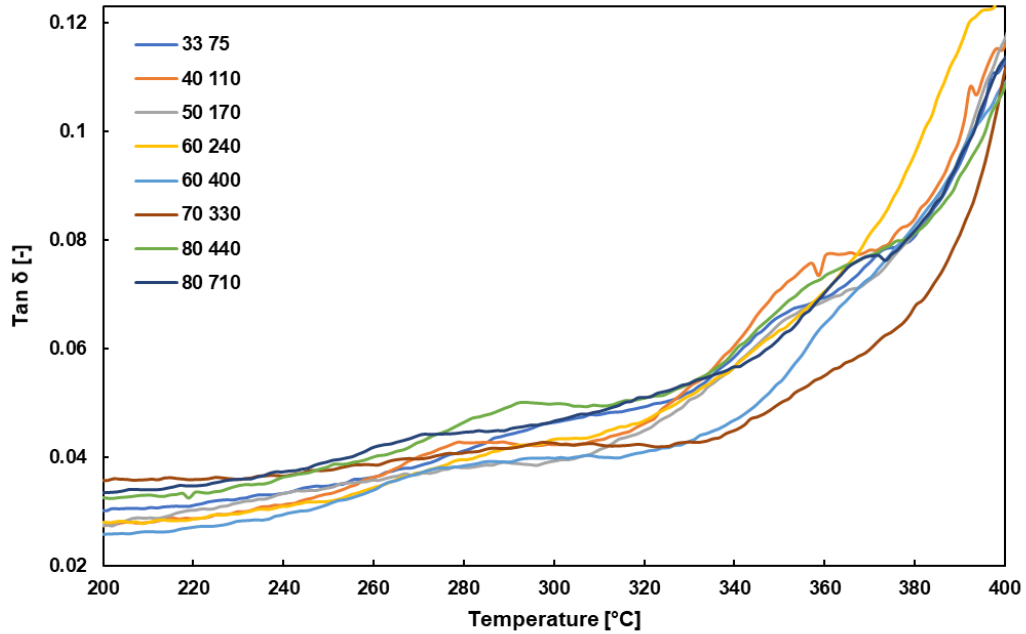


Figure 27: DMA results of all analyzed samples as a function of temperature between 200°C – 400°C, with emphasis on the relaxation behavior.

Just like when using DSC, it is also possible to predict T_g from DMA results. Therefore, the onset of T_g for all samples is evaluated as shown in Figure 28. The range is highly similar to DSC, where the onset of glass transition takes place between 392°C and 399°C in both cases. The trend itself is also comparable, in that a minimum T_g onset is observed when the energy density is between 60J/mm³ and 80J/mm³, increasing at lower and higher values.

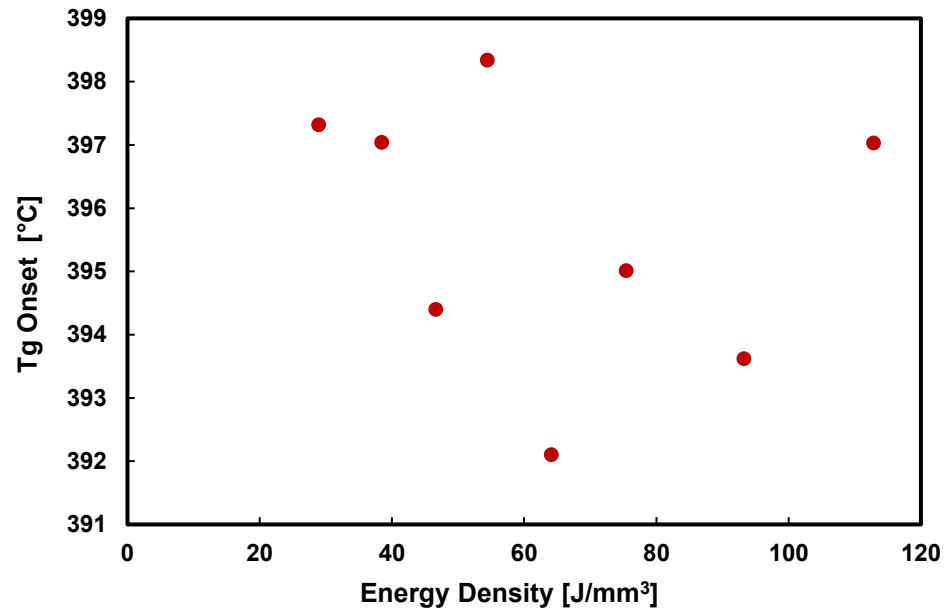


Figure 28: Onset of glass transition T_g with respect to energy density according to DMA results.

6 Discussion

6.1 Relaxation

A significant goal of this study is to optimize the thermal stability of AMZ4 throughout a broad temperature range. It is known that both T_g and T_x depend on the heating rate during processing, as proven in the results section. Furthermore, evidence exists suggesting that crystallization in phase-change materials is strongly linked to β -relaxation or the presence of a prominent excess wing in the loss modulus, occurring at a temperature lower than the glass transition temperature T_g and preceding the α -relaxation peak. [49] On an atomic level, it is said that β -relaxation is strongly related to the structural homogeneity as well as the atomic mobility of BMGs. [50] The experimental findings support the theoretical claims upon observation of the curves illustrated in Figure 27 that the processing conditions during additive manufacturing affect the relaxation. That is to say, not only do the results indicate signs of β -relaxation, they also show a dependence of energy density on the onset and prominence of relaxation, despite the inherent lack of a recognizable trend. These findings ultimately demonstrate that the varied process parameters will affect relaxation behavior, which may consequently have an influence on the thermal stability of the material.

As previously mentioned, it is known that BMG's tend to be considered brittle materials. Research however shows that the relationship between β -relaxation and the activation of shear transformation zones can be utilized to mitigate undesired brittleness. In essence, a pronounced β -relaxation peak may be indicative of macroscopic ductility at lower temperatures. Further, it is even suggested that certain mechanical properties may be predicted or tuned in accordance with activation of β -relaxations. [51] This is backed by the experimental outcomes, which support the fact that the degree of rejuvenation of a Zr-based metallic glass can in fact be adjusted. In summary, the applications of DMA as demonstrated in this study are promising, especially for the purpose of rejuvenation, when it can be used as a tool to probe the liquid-like volume in a BMG in order to enable ductility. To investigate this phenomenon further, future studies could be undertaken to compare the results of compression tests performed on two sets of printed samples, where one set is subjected to a form of thermal treatment such as annealing.

6.2 Model Validation

To ensure the accuracy of the conclusions drawn from the semi-analytical simulation, validation measures were implemented. In this case, particular emphasis was placed on the predicted degree of crystallinity. This was achieved by comparing the simulation results with XRD measurements and results from a previous study conducted by Z. Yang et al. [43]

As illustrated in Figure 29, previously conducted XRD measurements can be seen for all investigated energy densities, where the first number represents the laser power in watts and the second the scanning speed in mm/s. Common to almost all samples is the appearance of a broad hump near $2\theta=43^\circ$, indicating the presence of a predominantly amorphous structure. [38] The sample manufactured with a laser power of 70W and a scanning speed of 220mm/s stands out as an outlier. Unlike the other samples, this one exhibits prominent peaks along the curve, indicating the presence of crystal phases exceeding 5%. From a validation standpoint, these results agree well with the simulation model, considering the fact that the very same sample was predicted to have a crystal content of 10.83%, whereas all other samples contained less than 1% crystal volume fraction.

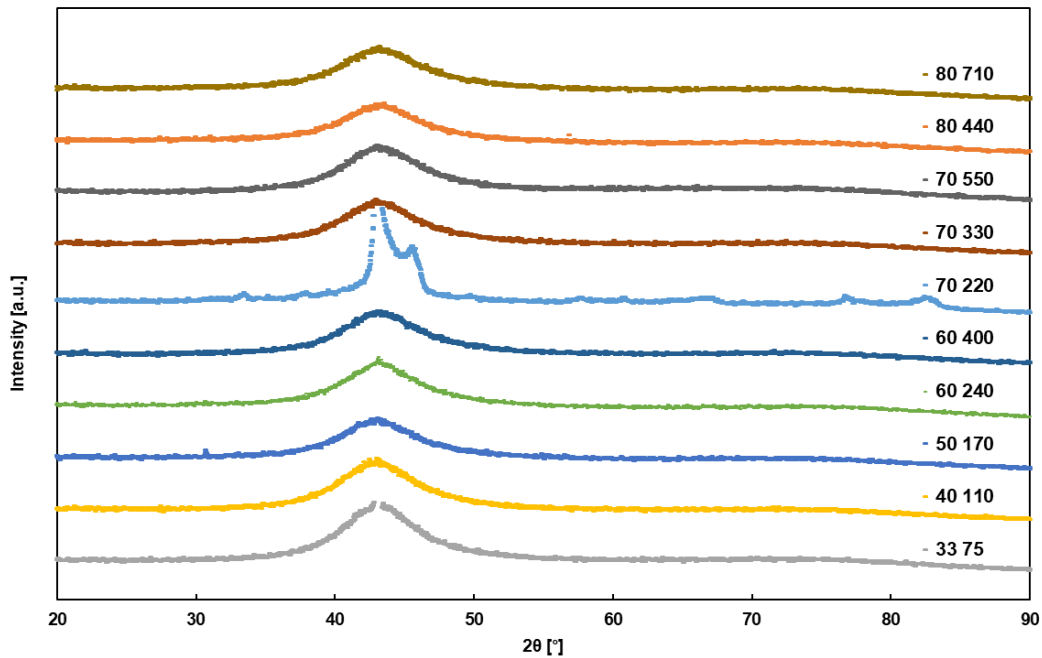


Figure 29: XRD results from previously conducted experiments for all analyzed samples.

As a secondary validation measure, the semi-analytical simulation model was compared against a model created by Yang et al. [43] The model is based on an experiment in which a single track is scanned repeatedly with a laser beam multiple times. Each single track was remelted for a different number of times, ranging from 1-25 in accordance with a step size of three. Three different laser power settings were used, namely 100W, 200W and 400W. The scanning speed and laser beam diameter were kept constant at 220mm/s and 500 μ m, respectively. In order to avoid heat accumulation, the laser was switched off for 30s between remelting cycles. Figure 30 provides a detailed overview of the experimental setup used by Yang. The numbers at the front of the sample represent the number of remelting cycles. [41] Yang's semi-analytical thermal model replicates one of the aforementioned experiments, with a laser power of 200W, 13 remelting cycles, and adequate cooling intervals to achieve a solution domain temperature prior to the next remelting cycle of $T_0=300$ K. For a more detailed overview of the boundary conditions used, refer to [43].

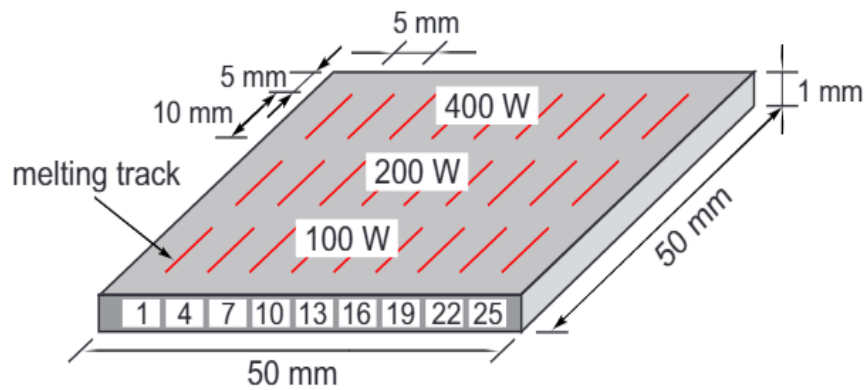


Figure 30: Experimental setup of a study conducted by Yang et al. in which the used laser power for each melting track is shown on the top surface and the number of remelting cycles is indicated on the front surface. [41]

In order to validate the in-house developed MATLAB model, slight adjustments were made to match Yang's simulation. The point of reference for a point located within the HAZ was positioned in the middle of the solution domain at a depth of 180 μ m. The laser beam radius, scan speed, and laser power were adjusted accordingly. To compensate for the increase in melt pool height over time, the point of reference was moved down 2 μ m after each remelting. The melt pool/HAZ boundary was defined as a function of the penetration depth equal to 147.5 μ m. 3.5s were chosen as an appropriate cooling time interval, leading to a total simulation time of approximately 45s. Despite the inherent temperature dependence on the specific heat capacity of AMZ4, this was taken as a constant ($c_p = 349$ J/kg K) in accordance with Yang's assumption. The coupled Nakamura model was also adjusted to simulate nucleation and growth at an oxygen content of 961ppm. For comparison sake, another solution was set up, in which the point of reference was inferred to be located within the melt pool, at a depth of 122.5 μ m beneath the surface. [43]

Figures 31 – 32 illustrate the results from both simulation models. Figures 31a – b represent the data obtained from a point located 180 μm below the top surface, while Figures 32a – b correspond to the data obtained from a point located 122.5 μm beneath the top surface. Regarding the former point, the results from both models are very similar. The first few seconds of run time boast peak temperatures of approximately 1200K, which drop to around 1000K after the remelting of the 13th layer due to the melt pool effect. The resulting degree of crystallinity of 60.4% obtained from the semi-analytical simulation model was also found to be in good agreement with Yang's model, with a discrepancy of less than 10%. At a shallower depth of 122.5 μm , the two models output similar thermal histories, beginning at an initial temperature of approximately 2000K after the first remelt, and gradually decaying after subsequent remelts. Despite the difference in order of magnitude with respect to the degree of crystallinity, the amount of crystals present is low enough such that it can be considered negligible. It must however, be stated, that only the Nakamura model can be compared in this case, due to the assumption that was made regarding the constant specific heat capacity. To put this into perspective, research suggests that the heat capacity of AMZ4 reaches almost 600J/kg K during glass transition, which strongly disagrees with the proposed 349J/kg K. [37, 41] After analyzing the XRD results and taking into account the results from third-party semi-analytical simulations, the developed model can be deemed valid, instilling confidence in its ability to qualitatively predict the degree of crystallinity in the laser powder bed fusion process for Zr-based metallic glasses.

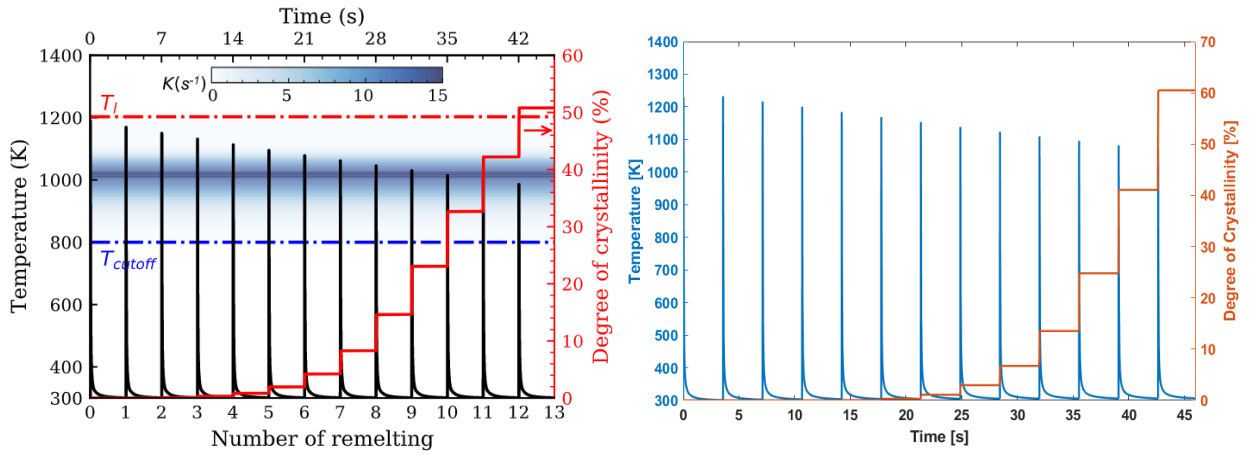


Figure 31: a) Degree of crystallinity at a point located $180\mu\text{m}$ below the top surface after 13 remelting cycles as simulated by Yang et al. [43] b) Degree of crystallinity at a point located $180\mu\text{m}$ below the top surface after 13 remelting cycles according to the developed simulation model.

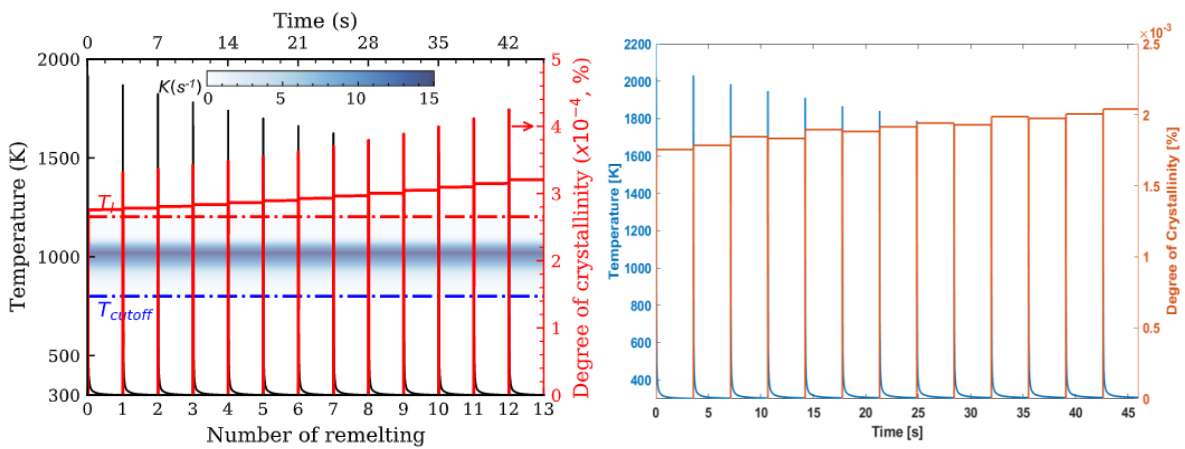


Figure 32: a) Degree of crystallinity at a point located $122.5\mu\text{m}$ below the top surface after 13 remelting cycles as simulated by Yang et al. [33] b) Degree of crystallinity at a point located $122.5\mu\text{m}$ below the top surface after 13 remelting cycles according to the developed simulation model.

6.3 Parameter Optimization

With the goal of optimizing the process parameters during additive manufacturing of AMZ4, three main criteria should be considered, namely the degree of crystallinity, the glass-forming ability and the thermal stability of the investigated samples. It is also noteworthy to mention the benefit of artificial intelligence (AI) with regard to further optimization efforts as a way to save time and costs. In summary, the optimized parameters may lead to improved mechanical properties in broader temperature ranges. [23, 52]

With reference to the results obtained from this study, it is necessary to establish which printing parameters lead to intolerable crystal content and vice versa. Both the simulation model as well as the corresponding XRD analysis infer crystal fractions of more than 5% when printing at 70W and 220mm/s. As a result of this large degree of crystallinity, these particular parameters can immediately be taken out of consideration. Contrarily, Figure 19 highlights in particular, three samples with crystal phases of less than 1×10^{-3} %. Each of these samples was manufactured with an energy density of less than 40 J/mm^3 , albeit with a variation in laser power ranging from 60W-80W and scanning speeds ranging from 400mm/s-710mm/s. Through qualitative inspection of the SEM results, one may conclude that they contain less crystal sites than any of the other samples analyzed. This visual evidence suggests that, to avoid unwanted crystallization, the energy density when manufacturing via LPBF should be less than 40 J/mm^3 .

To gain insight into the glass-forming ability as well as the thermal stability of this Zr-based BMG, it is recommended to turn to the DSC results, in particular Figure 24. The glass-forming ability, despite the quadratic relationship between energy density and ΔT_x , is highest at energy densities less than 50 J/mm^3 . In this case, the laser power for all three of these samples ranges from 60W-80W and the scanning speeds range from 400mm/s-710mm/s. Interestingly, these findings correspond well to those obtained from the evaluation regarding crystallization. The thermal stability, considered to be a function of ΔT_x , is exceptional for the samples mentioned above, when compared to the remainder of the tested samples. The superiority is largely attributed to not the onset of glass transition T_g , but the onset of crystallization T_x , ranging from 474°C - 475°C , which is on average 10°C higher compared to the other samples.

An overview of the most favorable process parameters complying with the conclusions made above is depicted in Table 7. To summarize, it is possible to conclude that the commercial, intended use of additively manufactured AMZ4 is indeed possible, albeit at energy densities within the range of 28J/mm³-38J/mm³.

Table 7: Overview of the three best performing samples with respect to the degree of crystallinity and glass-forming ability.

Laser Power [W]	Scan Speed [mm/s]	Energy Density [J/mm³]	Relative Density [%]	Degree of Crystallinity [%]	ΔT_x [°C]
60	400	38.46	99.94	5 x 10 ⁻⁴	76
70	550	32.63	99.93	8.8 x 10 ⁻⁵	-
80	710	28.89	99.95	6.9 x 10 ⁻⁶	77

Although the primary focus of this study is to optimize the laser power as well as the scan speed, many other variables such as the hatching distance and layer thickness can undoubtedly also be adjusted to further improve the properties of the alloy [53]. The porosity for example, is a property that was evaluated manually using OM during the preliminary parameter selection process. The current MATLAB model is incapable of predicting porosity, which, if implemented, could help save a substantial amount of time when characterizing similar alloys, by circumventing the need to print samples of potentially poor quality. Such efforts could be taken a step further, through the use of machine learning (ML), where appropriate. For instance, by varying the sample dimensions, beam diameter, or hatching distance, the effects on the percent crystallinity and porosity of the produced part can be determined. The outcomes of these analyses could then be used as input data for artificial neural networks. From here, the user would simply need to select the parameters to be optimized, which in this case refer to the crystallization kinetics and relative density. The neural network is then able to numerically predict the magnitudes of the process parameters required to minimize crystallinity and maximize density. [54] The advantages of using AI for such an application include the decrease in computation time through reducing the number of required simulations, as well as the ability to reduce the amount of carried out experiments through virtual development and characterization.

7 Conclusion

Zr-based bulk metallic glasses are newly emerging, highly advanced engineering materials with several promising applications, especially within the biomedical industry. [55] Despite benefiting from the high cooling rates offered when manufacturing via selective laser melting, continuous reheating during the process leads to unwanted degradation of the materials properties. Therefore, there exists an inherent need to optimize the process parameters in order to be able to produce parts of high quality. This study employs a series of different experiments, as well as an in-house developed simulation algorithm with means to define the relationship between process parameters such as the energy density and the relaxation and crystallization behavior of AMZ4.

The aim of this work was achieved by having first and foremost, conducted a preliminary parameter selection study by eliminating the samples with unsuitably high levels of porosity. The parameters that were varied were strictly limited to laser power and scan speed, and the porosities of all samples selected for further analysis were under 0.1%. This was done to ensure that the resulting mechanical properties of the specimens corresponded to the theoretical limits mentioned in the reviewed literature. It was furthermore found that, while the relative density increases with increasing energy density, the effect can be considered as negligible from about 40J/mm^3 onwards.

This optimization method was followed by a series of experiments including SEM, DSC and DMA, designed to provide insight into the presence of crystals, thermal stability and relaxation characteristics, respectively. While the DSC analyses provided information on the relaxation and crystallization enthalpies, they were mainly used for defining T_g and T_x , which are the most important factors in determining the glass-forming ability. It was found that energy densities of less than 50J/mm^3 were required to achieve optimal thermal stability. Although the SEM results provided useful insights by confirming the presence of crystals in nearly all samples, they were insufficient for providing quantitative conclusions, which led to the decision to consider them secondary to, for example, the DSC results, in terms of reliability. Finally, the DMA test results revealed substantial variations in β -relaxation behavior based on energy density, indicating the potential for optimizing BMG relaxation by fine-tuning the process. In future studies, this could be further elaborated to increase the benefit of this type of rejuvenation and to further confirm it by mechanical testing.

The development of a semi-analytical model, which can calculate the temperature and degree of crystallinity at arbitrary points within a sample without relying on full-scale FEM models, is a crucial contribution to this work. In using such a tool, the amount of time-consuming experiments such as XRD measurements can be significantly reduced. Moreover, the model was validated against not

only previously performed XRD experiments, but also results from the literature. The multi-track simulations were therefore used, in conjunction with the DSC results, to select the three best samples by optimizing for minimum crystal content and the maximum thermal stability. The outcomes, provided the porosity levels are acceptable, support the initial hypothesis that lower energy densities ($<40\text{J/mm}^3$) do in fact lead to increased amorphous content.

Although the primary focus of this work was to optimize the laser power and scan speed, other variables such as the hatching distance and layer thickness could also be adjusted in future studies, to further improve the properties of the alloy. However, it is important to keep in mind that increasing the number of variables will lead to increased complexity. Therefore, it is recommended to couple the current MATLAB model with an ML algorithm to help predict the process parameters required to minimize crystallinity and maximize density for given input variables including hatching distance and layer thickness. This initiative will help material scientists accelerate the development of AMZ4 and other metallic glasses through a reduction in experiments, as well as simulation loops.

In summary, this thesis has contributed to the understanding of the effects of process parameters on the degree of crystallinity, porosity, and thermal stability of AMZ4 samples manufactured via LPBF. The findings suggest that energy density plays a crucial role in avoiding unwanted crystallization, and the use of a semi-analytical simulation model can aid in predicting crystal percentages. Moreover, the use of ML could further improve the optimization of process parameters. Overall, the findings of this study can be used to optimize the manufacturing process of AMZ4 and improve its mechanical and thermal properties, making it a promising candidate for commercial use.

8 References

- [1] C. Suryanarayana und A. Inoue, „Metallic Glasses,“ July 2012.
- [2] M. Telford, „The case for bulk metallic glass,“ *Materials Today*, Bd. 7, p. 36–43, March 2004.
- [3] M. Bakkal, U. Karagüzel und A. T. Kuzu, „Manufacturing Techniques of Bulk Metallic Glasses,“ p. 137–148, August 2019.
- [4] N. Sohrabi, J. Jhabvala, G. Kurtuldu, R. Frison, A. Parrilli, M. Stoica, A. Neels, J. F. Löffler und R. E. Logé, „Additive manufacturing of a precious bulk metallic glass,“ *Applied Materials Today*, Bd. 24, p. 101080, 2021.
- [5] D. C. Hofmann, „Bulk Metallic Glasses and Their Composites: A Brief History of Diverging Fields,“ *Journal of Materials*, Bd. 2013, p. 1–8, January 2013.
- [6] M. Pontoreau, O. Dezellus, S. Cardinal, J.-M. Pelletier, R. Chiriac, F. Toche, P. Steyer, L. Gremillard, M. Vallée und X. Boulnat, „Towards the additive manufacturing of Zr-based metallic glasses using liquid phase sintering: Reactivity and phase transformation kinetics at the crystalline/amorphous interface,“ *Journal of Alloys and Compounds*, Bd. 962, p. 171179, November 2023.
- [7] W. KLEMENT, R. H. WILLENS und P. O. L. DUWEZ, „Non-crystalline Structure in Solidified Gold–Silicon Alloys,“ *Nature*, Bd. 187, p. 869–870, September 1960.
- [8] C. A. Schuh, T. C. Hufnagel und U. Ramamurty, „Mechanical behavior of amorphous alloys,“ *Acta Materialia*, Bd. 55, pp. 4067-4109, 2007.
- [9] N. Sohrabi, J. Jhabvala und R. E. Logé, „Additive Manufacturing of Bulk Metallic Glasses—Process, Challenges and Properties: A Review,“ *Metals*, Bd. 11, 2021.
- [10] F. Spaepen, „A microscopic mechanism for steady state inhomogeneous flow in metallic glasses,“ *Acta Metallurgica*, Bd. 25, pp. 407-415, 1977.
- [11] S. K. Patel, B. K. Swain, A. Behera und S. S. Mohapatra, „Metallic Glasses: A Revolution in Material Science,“ February 2020.
- [12] F.-F. Cai, B. Sarac, Z. Chen, C. Czibula, F. Spieckermann und J. Eckert, „Surmounting the thermal processing limits: Patterning TiZrCuPdSn bulk metallic glass even with nanocrystallization,“ *Materials Today Advances*, Bd. 16, p. 100316, 2022.
- [13] J. Wegner, M. Frey, M. Piechotta, N. Neuber, B. Adam, S. Platt, L. Ruschel, N. Schnell, S. S. Riegler, H.-R. Jiang, G. Witt, R. Busch und S. Kleszczynski, „Influence of powder characteristics on the structural and the mechanical properties of additively manufactured Zr-based bulk metallic glass,“ *Materials & Design*, Bd. 209, p. 109976, 2021.

- [14] M. Stolpe, „HERSTELLUNG EINES METALLISCHEN MASSIVGLAS-KOMPOSITMATERIALS MITTELS PULVERBASIERTER, ADDITIVER FERTIGUNG“. Germany Patent EP 3 542 925 A1, 25 September 2019.
- [15] N. Sohrabi, A. Parrilli, J. Jhabvala, A. Neels und R. E. Logé, „Tensile and Impact Toughness Properties of a Zr-Based Bulk Metallic Glass Fabricated via Laser Powder-Bed Fusion,“ *Materials*, Bd. 14, p. 5627, September 2021.
- [16] N. Sohrabi, J. Jhabvala, G. Kurtuldu, M. Stoica, A. Parrilli, S. Berns, E. Polatidis, S. V. Petegem, S. Hugon, A. Neels, J. F. Löffler und R. E. Logé, „Characterization, mechanical properties and dimensional accuracy of a Zr-based bulk metallic glass manufactured via laser powder-bed fusion,“ *Materials & Design*, Bd. 199, p. 109400, 2021.
- [17] S. A. M. Tofail, E. P. Koumoulos, A. Bandyopadhyay, S. Bose, L. O'Donoghue und C. Charitidis, „Additive manufacturing: scientific and technological challenges, market uptake and opportunities,“ *Materials Today*, Bd. 21, pp. 22-37, 2018.
- [18] S. Chowdhury, N. Yadaiah, C. Prakash, S. Ramakrishna, S. Dixit, L. R. Gupta und D. Buddhi, „Laser powder bed fusion: a state-of-the-art review of the technology, materials, properties & defects, and numerical modelling,“ *Journal of Materials Research and Technology*, Bd. 20, pp. 2109-2172, 2022.
- [19] D. D. Singh, T. Mahender und A. R. Reddy, „Powder bed fusion process: A brief review,“ *Materials Today: Proceedings*, Bd. 46, p. 350–355, 2021.
- [20] F. Galbusera, L. Caprio, B. Previtali und A. G. Demir, „The influence of novel beam shapes on melt pool shape and mechanical properties of LPBF produced Al-alloy,“ *Journal of Manufacturing Processes*, Bd. 85, pp. 1024-1036, 2023.
- [21] W. H. Kan, L. N. S. Chiu, C. V. S. Lim, Y. Zhu, Y. Tian, D. Jiang und A. Huang, „A critical review on the effects of process-induced porosity on the mechanical properties of alloys fabricated by laser powder bed fusion,“ *Journal of Materials Science*, Bd. 57, p. 9818–9865, March 2022.
- [22] J. M. Ravalji und S. J. Raval, „Review of quality issues and mitigation strategies for metal powder bed fusion,“ *Rapid Prototyping Journal*, Bd. 29, p. 792–817, October 2022.
- [23] N. Hua, Z. Liao, Q. Wang, L. Zhang, Y. Ye, J. Brechtl und P. K. Liaw, „Effects of crystallization on mechanical behavior and corrosion performance of a ductile Zr68Al8Ni8Cu16 bulk metallic glass,“ *Journal of Non-Crystalline Solids*, Bd. 529, p. 119782, 2020.
- [24] N. Sohrabi, M. Hamidi-Nasab, B. Rouxel, J. Jhabvala, A. Parrilli, M. Vedani und R. E. Logé, „Fatigue Performance of an Additively Manufactured Zr-Based Bulk Metallic Glass and the Effect of Post-Processing,“ *Metals*, Bd. 11, p. 1064, July 2021.
- [25] X. Wu, S. Lan, X. Wei, J. Zhou, Z. Lu, J. D. Almer und X.-L. Wang, „Elucidating the nature of crystallization kinetics in Zr46Cu46Al8 metallic glass through simultaneous WAXS/SAXS measurements,“ *Applied Physics Letters*, Bd. 114, May 2019.

- [26] Sohrabi, Navid and Schawe, Jürgen E.K. and Jhabvala, Jamasp and Löffler, Jörg F. and Logé, Roland E., "Critical crystallization properties of an industrial-grade Zr-based metallic glass used in additive manufacturing," 2021.
- [27] P. Zhang, J. Tan, Y. Tian, H. Yan und Z. Yu, „Research progress on selective laser melting (SLM) of bulk metallic glasses (BMGs): a review,“ *The International Journal of Advanced Manufacturing Technology*, Bd. 118, p. 2017–2057, September 2021.
- [28] B. Bochtler, "Thermophysical and structural investigations of a CuTi- and a Zr-based bulk metallic glass, the influence of minor additions, and the relation to thermoplastic forming," 2019.
- [29] S. Karthika, T. K. Radhakrishnan und P. Kalaichelvi, „A Review of Classical and Nonclassical Nucleation Theories,“ *Crystal Growth & Design*, Bd. 16, p. 6663–6681, November 2016.
- [30] A. Ericsson, V. Pacheco, M. Sahlberg, J. Lindwall, H. Hallberg und M. Fisk, „Transient nucleation in selective laser melting of Zr-based bulk metallic glass,“ *Materials & Design*, Bd. 195, p. 108958, 2020.
- [31] J. Lindwall, „Modelling of laser-based powder bed fusion for bulk metallic glass formation,“ 2021.
- [32] Y. Shen, Y. Li und H.-L. Tsai, „Evolution of crystalline phase during laser processing of Zr-based metallic glass,“ *Journal of Non-Crystalline Solids*, Bd. 481, pp. 299-305, 2018.
- [33] P. Kejzlar, M. Švec und E. Macajová, „The Usage of Backscattered Electrons in Scanning Electron Microscopy,“ *Manufacturing Technology*, Bd. 14, p. 333–336, October 2014.
- [34] S. R. Aubuchon, „Dynamic Mechanical Analysis Under Controlled Conditions of Temperature and Relative Humidity,“ *American Laboratory*, 2009.
- [35] P. Zagade, B. P. Gautham, A. De und T. DebRoy, „Analytical estimation of fusion zone dimensions and cooling rates in part scale laser powder bed fusion,“ *Additive Manufacturing*, Bd. 46, p. 102222, October 2021.
- [36] N. T. Nguyen, A. Ohta, K. Matsuoka, N. Suzuki und Y. Maeda, „Analytical Solutions for Transient Temperature of Semi-Infinite Body Subjected to 3-D Moving Heat Sources,“ *The Welding Journal*, 1999.
- [37] J. Lindwall, V. Pacheco, M. Sahlberg, A. Lundbäck und L.-E. Lindgren, „Thermal simulation and phase modeling of bulk metallic glass in the powder bed fusion process,“ *Additive Manufacturing*, Bd. 27, p. 345–352, May 2019.
- [38] J. J. Marattukalam, V. Pacheco, D. Karlsson, L. Riekehr, J. Lindwall, F. Forsberg, U. Jansson, M. Sahlberg und B. Hjörvarsson, „Development of process parameters for selective laser melting of a Zr-based bulk metallic glass,“ *Additive Manufacturing*, Bd. 33, p. 101124, 2020.

- [39] J. J. Segovia, D. Lozano-Martín, M. C. Martín, C. R. Chamorro, M. A. Villamañán, E. Pérez, C. G. Izquierdo und D. del Campo, „Updated determination of the molar gas constant R by acoustic measurements in argon at UVa-CEM,“ *Metrologia*, Bd. 54, p. 663–673, August 2017.
- [40] M. Becker, A. Kuball, A. Ghavimi, B. Adam, R. Busch, I. Gallino und F. Balle, „Solid State Joining of a Cold Rolled Zr-Based Bulk Metallic Glass to a Wrought Aluminum Alloy by Power Ultrasonics,“ *Materials*, Bd. 15, 2022.
- [41] Z. Yang, H. Wang, S. Krauß, F. Huber, B. Merle, M. Schmidt, M. Markl und C. Körner, „Evolution of an industrial-grade Zr-based bulk metallic glass during multiple laser beam melting,“ *Journal of Non-Crystalline Solids*, Bd. 589, p. 121649, 2022.
- [42] B. B. Ravichander, K. Mamidi, V. Rajendran, B. Farhang, A. Ganesh-Ram, M. Hanumantha, N. S. Moghaddam und A. Amerinatanzi, „Experimental investigation of laser scan strategy on the microstructure and properties of Inconel 718 parts fabricated by laser powder bed fusion,“ *Materials Characterization*, Bd. 186, p. 111765, 2022.
- [43] Z. Yang, M. Markl und C. Körner, „Predictive simulation of bulk metallic glass crystallization during laser powder bed fusion,“ *Additive Manufacturing*, Bd. 59, p. 103121, 2022.
- [44] N. Wang, S. Chang, G. Li, S. T. Dheen, A. S. Kumar, W. Wu, Q. Liu, J. Zhao, L. Ren und J. Y. H. Fuh, „Effects of Various Processing Parameters on Mechanical Properties and Biocompatibility of Fe-based Bulk Metallic Glass Processed via Selective Laser Melting at Constant Energy Density,“ *Chinese Journal of Mechanical Engineering: Additive Manufacturing Frontiers*, Bd. 1, p. 100038, 2022.
- [45] S. V. Madge und A. L. Greer, „Laser additive manufacturing of metallic glasses: issues in vitrification and mechanical properties,“ *Oxford Open Materials Science*, Bd. 1, November 2020.
- [46] M. Biały, M. Hasiak und A. Łaszcz, „A Novel Approach to Analysis of Complex Crystallization Behavior in Zr-Based Bulk Metallic Glass by Non-isothermal Kinetics Studies,“ *Metallurgical and Materials Transactions A*, Bd. 54, p. 1428–1442, 2023.
- [47] K. Gruszka, M. Nabiałek, M. Szota, K. Bloch, J. Gondro, P. Pietrusiewicz, A. V. Sandu, A. M. M. A. Bakri, S. Walters, K. Walters, S. Garus, M. Dośpiał und J. Mizera, „Analysis of the Thermal and Magnetic Properties of Amorphous Fe₆₁Co₁₀Zr_{2.5}Hf_{2.5}Me₂W₂B₂₀ (Where Me = Mo, Nb, Ni Or Y) Ribbons,“ *Archives of Metallurgy and Materials*, Bd. 61, p. 641–644, June 2016.
- [48] K. Hazeli, A. Sadeghi, M. O. Pekguleryuz und A. Kontsos, „Damping and dynamic recovery in magnesium alloys containing strontium,“ *Materials Science and Engineering: A*, Bd. 589, p. 275–279, January 2014.
- [49] Y. Cheng, Q. Yang, J. Wang, T. Dimitriadis, M. Schumacher, H. Zhang, M. J. Müller, N. Amini, F. Yang, A. Schoekel, J. Pries, R. Mazzarello, M. Wuttig, H.-B. Yu und S. Wei, „Highly

tunable β -relaxation enables the tailoring of crystallization in phase-change materials," *Nature Communications*, Bd. 13, p. 7352, 2022.

- [50] B. Bian, X. Cui und J. Li, „Long-term thermal stability, β relaxation, and mechanical behavior of a {LaCe}-based bulk metallic glass," *AIP Advances*, Bd. 11, p. 015202, January 2021.
- [51] H.-B. Yu, W.-H. Wang und K. Samwer, „The β relaxation in metallic glasses: an overview," *Materials Today*, Bd. 16, pp. 183-191, 2013.
- [52] S. Theeda, S. H. Jagdale, B. B. Ravichander und G. Kumar, „Optimization of Process Parameters in Laser Powder Bed Fusion of SS 316L Parts Using Artificial Neural Networks," *Metals*, Bd. 13, 2023.
- [53] A. Maamoun, Y. Xue, M. Elbestawi und S. Veldhuis, „Effect of Selective Laser Melting Process Parameters on the Quality of Al Alloy Parts: Powder Characterization, Density, Surface Roughness, and Dimensional Accuracy," *Materials*, Bd. 11, p. 2343, November 2018.
- [54] Z. Jin, Z. Zhang, K. Demir und G. X. Gu, „Machine Learning for Advanced Additive Manufacturing," *Matter*, Bd. 3, pp. 1541-1556, 2020.
- [55] J. A. Horton und D. E. Parsell, „Biomedical Potential of a Zirconium-Based Bulk Metallic Glass," *MRS Proceedings*, Bd. 754, 2002.

9 Appendix

9.1 Linearization of C_p

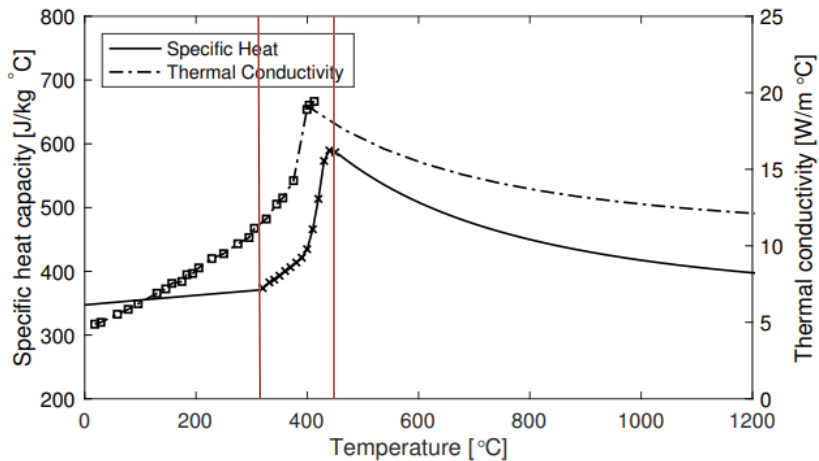
The linearization of the specific heat capacity c_p of AMZ4, with respect to the four regions referred to in the methods section, will be demonstrated for the transition region where $320^\circ\text{C} \leq T < 420^\circ\text{C}$. Referencing the region marked in red of the graph below, the c_p at 320°C is about $370\text{J/kg}^\circ\text{C}$, whereas the c_p at 420°C can be estimated to be $600\text{J/kg}^\circ\text{C}$. Using the slope of a line formula, the slope m can be defined as follows:

$$m = (c_{p,2} - c_{p,1}) / (T_2 - T_1)$$

In this case, $m=2.3$. Converting the temperature to Kelvin provides $T_1=493\text{K}$ and $T_2=693\text{K}$. The equation of a line must now be used as shown:

$$c_{p,2} = 2.3T_2 + b$$

b is the y-intercept, and can be considered equal to c_{p0} . Solving the equation gives $c_{p0} = -993.9$. The same procedure is followed for determining the other material constants.



9.2 Single-Track Model

```
clear all
close all
clc

P=30; % Laser power (W)
v=0.075; % Scan Speed (m/s)
vy=0; % Scan Speed y (m/s)
rb=.000040; %Laser beam radius (m)
n=0.35; %Absorption coefficient
rho=6640; %Density
alpha=0.0000021; %Diffusivity
cp0=240; %Material constant 1
m=0.0018; %Material constant 2
fp=3; %Beam distribution parameter 1
fd=3; %Beam distribution parameter 2
T0=298; %Ambient temperature (K)
R=8.314; %Molar gas constant
Ts=1150; %Solidus temperature (K)
C=462; %Specific heat @ solidus T

ts=0.001; %Starting time
tend=0.025; %End time

parameters=[33 40 50 60 60 70 70 70 80 80;...
            .075 .11 .17 .24 .4 .22 .33 .55 .44 .71];

%Generation of arrays for heating/cooling rates
Heating_Rate=zeros(10,1);
Cooling_Rate=zeros(10,1);

for l=1:10

    P=parameters(1,l);
    v=parameters(2,l);

    formatSpec="%5.0f%5.0f";
    plotHandles{l}=sprintf(formatSpec,P,v*1000);

    par=v*0.1*tend; %Parameter for x position (m)

    %Logarithmically scaled time step (s)
    t=logspace(log10(0.001),log10(tend),1024);

    %Starting coordinates of laser (x,y,z)
    xs=0;
    ys=0;
    x=par;
    z=-0.000015;
    y=0;

    j=1:128;
    ctr=1;

    Temp=zeros(numel(i),numel(i)); %Array for Temperature
    Spec_Heat=zeros(numel(i),numel(i)); %Array for Specific Heat

    P1=zeros(1,2); %X1 & Y1 for determining slope (Section I)
    P2=zeros(1,2); %X2 & Y2 for determining slope (Section I)
    P3=zeros(1,2); %X2 & Y2 for determining slope (Section II)
```

```

i=1:1024;
for i=i

    ts=t(i);

    %Assumption: There is no y displacement

    %Definition of melt pool height (m)
    h=0.08*(((n*P*(rb/v))/(pi*rb^2*sqrt(alpha*rb/v)*(rho*C*Ts)))^1.4)*rb;

    k=1;
    delta=150;
    while delta>1

        %Heat input per time step
        T=@(t2)(2*fp*n*P*sqrt(fd))/(rho*cp0*pi*sqrt(pi)...
            .*((4*fp*alpha*(ts-t2)+rb^2)...
            .*sqrt(4*fd*alpha*(ts-t2)+h^2))).*exp(-fp*((x-(xs+v*t2))...
            .^2+(y-(ys+vy*t2)).^2)/(4*fp*alpha*(ts-t2)+rb^2)...
            -((fd*z^2)/(4*fd*alpha*(ts-t2)+h^2)));

        q=integral(T,0,ts);

        %Temperature at point of interest (K)
        Tnew(k)=((sqrt(2*m*q+((1+m*T0)^2)))-1)./m;

        %If-statements for linearization of specific heat
        if (Tnew(k)>=693 && Tnew(k)<1473)
            m=-0.000329; % Specific heat at glassy state
            cp0=777.69213;

        elseif (Tnew(k)>=593 && Tnew(k)<693) % Specific heat
            % at transition state
            m=-0.002314;
            cp0=-993.9;

        elseif (Tnew(k)<593)
            m=0.0002; % Specific heat at liquid state
            cp0=331.709;

        else
            m=((400/331.709)-1)/Tnew(k);
            cp0=331.709;

        end

        if k>1
            delta=abs(Tnew(k-1)-Tnew(k));

        end

        Cp(k)=cp0*(1+m*Tnew(k));

        %Adjusting specific heat for convergence
        if k>1 && Cp(k)>Cp(k-1)
            Cp(k)=Cp(k)-0.99*(Cp(k)-Cp(k-1));
        end

        m=((Cp(k)/331.709)-1)/Tnew(k);

        cp0=331.709;

        k=k+1;
    end

    % If-Statements for slope (heating/cooling rates)

    if i==1

```

```

        P1(1,1)=0;
        P1(1,2)=Tnew(k-1)-273;

    end

    if i==1023

        [val, ind]=max(Temp(1,:));
        P2(1,2)=val;
        P2(1,1)=t(ind);

    end

    if Tnew(k-1)<663 && v*t(i)>x && P3(1,1)==0
        P3(1,1)=t(i);
        P3(1,2)=Tnew(k-1)-273;
    end

    Tnew=Tnew(k-1);
    Temp(j,ctr)=Tnew-273;
    Spec_Heat(j,ctr)=Cp(k-1);
    ctr=ctr+1;

end

ctr=1;
ts=0.00025;

%Plotting of results
plot(t,Temp(1,:))
xlabel('Time [s]')
ylabel('Temperature [°C]')
title('Thermal History (Single Track)')
legend(plotHandles);
hold on

Heating_Rate(1)=(P1(1,2)-P2(1,2))/(P1(1,1)-P2(1,1)); %Slope Section I
Cooling_Rate(1)=(P2(1,2)-P3(1,2))/(P2(1,1)-P3(1,1)); %Slope Section II

end

Parameters=transpose(["3375", "40110", "50170", "60240", "60400", "70220", ...
    "70330", "70550", "80440", "80710"]);

data=table(Parameters,Heating_Rate,Cooling_Rate);

```

Published with MATLAB® R2022b

9.3 Single-Track Validation

```
clear all
close all
clc

P=200; % Laser power (w)
vx=0.2; % Scan Speed x (m/s)
vy=0; % Scan Speed y (m/s)
rb=.00025; %Laser beam radius (m)
n=0.35; %Absorption coefficient
rho=6640; %Density
alpha=0.0000021; %Diffusivity
cp0=330; %Material constant 1
m=0.000083; %Material constant 2
fp=3; %Beam distribution parameter 1
fd=3; %Beam distribution parameter 2
T0=298; %Ambient temperature (K)
R=8.314; %Molar gas constant
Ts=1150; %Solidus temperature (K)
C=435; %Specific heat @ solidus T
M=0.076595; %Molar mass of AMZ4
layers=1; %Number of layers
Cp=349; %Specific heat capacity (J/kgK)

parameters=[200 40 50 60 60 70 70 80 80;...
            .2 .11 .17 .24 .4 .22 .33 .55 .44 .71];

for l=1

    %Definition of laser power and scan speed
    P=parameters(1,l);
    vx=parameters(2,l);

    formatSpec="%5.0f%5.0f";
    plotHandles{1}=sprintf(formatSpec,P,vx*1000);

    xs=0;
    ys=0;
    z=-0.0001225; %Initial depth of solution domain (m)
    y=0;

    ctr=1;
    i=1:layers*45000;
    j=1;

    Temp=zeros(1,numel(i)); %Array for Temperature
    Temp2=zeros(1,numel(j)); %Array for Temperature for Nakamura model
    N=zeros(1,numel(i)+1); %Nakamura Matrix
    Spec_Heat=zeros(1,numel(i)); %Array for Specific Heat

    % Conditions controlling loops in accordance with sample width
    width=0; %Sample width
    dy=0.00013; %Hatching distance
    tracks=13; %Number of tracks required
    tracks=round(tracks);
    q=zeros(1,tracks*layers);
    q=transpose(q);

    %Conditions for starting times per track
    length=0.01; %Length of sample (x)
    ts1=length/vx+3.5; %Starting time of first track (s)
    t_end=(tracks*layers)*ts1;
    ts=linspace(ts1,t_end,tracks*layers);
    ts=transpose(ts);

    %Definition of location of solution domain
    par=0.5;
    x=(vx*(ts1-3.5))*par;
```

```

%Definition of time step
time=linspace(0.00025,t_end, layers*45000);
delta_t=time(1,3)-time(1,2);

for i=i

    t=time(i);
    h=0.0001475; %Melt pool height (m)
    k=1;
    delta=150;
    while delta>0.1

        b=1;
        c=1;

        while t>ts(b)

            v=vx;
            xs=0;

            %Heat input per time step
            T=@(t2)1./((4*fp*alpha*(t-t2)+rb^2)...
                .*sqrt(4*fd*alpha*(t-t2)+h^2))...
                .*exp(-fp*((x-(xs+v*(t2-ts(b))))...
                .^2+(y-(ys+vy*(t2-ts(b))))).^2)...
                ./((4*fp*alpha*(t-t2)+rb^2)-((fd*z^2)...
                ./((4*fd*alpha*(t-t2)+h^2))));

            q(c)=integral(T,ts(b),t);

            c=c+1;
            b=b+1;
            %Adjusting depth of thermal field due to melt pool effect
            z=z-0.000002;

        end

        %Heat input from Track 1
        z=-0.0001225;
        v=vx;
        xs=0;
        ys=0;

        T_old=@(t2)1./((4*fp*alpha*(t-t2)+rb^2)...
            .*sqrt(4*fd*alpha*(t-t2)+h^2))...
            .*exp(-fp*((x-(xs+v*t2)).^2+(y-(ys+vy*t2)).^2)...
            ./((4*fp*alpha*(t-t2)+rb^2)-((fd*z^2)...
            -((fd*z^2)./(4*fd*alpha*(t-t2)+h^2))));

        q(c)=integral(T_old,0,t);

        %Sum of heat input from all tracks
        Q=sum(q)*(2*fp*n*P*sqrt(fd)*2*m)./(rho*cp0*pi*sqrt(pi));

        %Temperature at point of interest
        Tnew(k)=((sqrt(Q+((1+m*T0)^2)))-1)./m;

        if k>1
            delta=abs(Tnew(k-1)-Tnew(k));

        end
        m=((Cp/cp0)-1)/Tnew(k);
        mat(k)=m;

        %Adjusting material constant for convergence
        if k>1 && mat(k)>mat(k-1)
            mat(k)=mat(k)-0.99*(mat(k)-mat(k-1));
        end

        k=k+1;
    end

    m=0.000083;

    Tnew=Tnew(k-1);

```

```

Temp(i)=Tnew-273;
Temp2(j)=Tnew;

%Determining degree of crystallinity using Nakamura model
if j==1
    N(j)=0;
    X(j)=0;

elseif Temp2(j)>1200
    N(j)=0;
    X(j)=0;

else
    N(j)=N(j-1)+delta_t*Nakamura_model_961(Temp2(j-1));
    X(j)=X(j-1)+delta_t*4*Nakamura_model_961(Temp2(j-1))*...
        exp(-(N(j))^4)*N(j)^3;
end

ctr=ctr+1;
j=j+1;

end

ctr=1;

timenew=time;

%Plotting of results
yyaxis left
plot(time,Temp+273)
xlabel('t [s]')
ylabel('Temperature [K]')
hold on
yyaxis right
plot(time,X*100)
ylabel('Degree of Crystallinity [%]')

Heating_Rate(1)=(P1(1,2)-P2(1,2))/(P1(1,1)-P2(1,1)); %Slope Section I
Cooling_Rate(1)=(P2(1,2)-P3(1,2))/(P2(1,1)-P3(1,1)); %Slope Section II

end

Parameters=transpose(["3375", "40110", "50170", "60240", "60400", "70220", ...
    "70330", "70550", "80440", "80710"]);

```

Published with MATLAB® R2022b

9.4 Multi-Track Model

```
function AMZ4_20230328_multi_track_function...
(P,vx, layers, length, width, x, dy, H, y)

%Global variables are user defined via GUI
global P vx layers length width x dy H y

vy=0; % Scan Speed y (m/s)
rb=.000040; %Laser beam radius (m)
n=0.35; %Absorption coefficient
rho=6640; %Density (kg/m^3)
alpha=0.0000021; %Diffusivity (m^2/s)
cp0=331; %Material constant 1
m=0.0002; %Material constant 2
fp=3; %Beam distribution parameter 1
fd=3; %Beam distribution parameter 2
T0=298; %Ambient temperature (K)
R=8.314; %Molar gas constant
Ts=1150; %Solidus temperature (K)
C=462; %Specific heat @ solidus T
f=10000; %Time steps per layer
depth=0.001; %Depth of sample (m)

parameters=[33 40 50 60 60 70 70 70 80 80;...
            .075 .11 .17 .24 .4 .22 .33 .55 .44 .71];

for l=1

    xs=0;
    ys=0;
    zs=0;

    % Conditions controlling loops in accordance with sample width

    tracks=width/dy+1; %Number of tracks required
    tracks=round(tracks);
    q=zeros(1,tracks*layers);
    q=transpose(q);

    %Conditions for starting times per track
    ts1=length/vx; %Starting time of first track (s)
    t_end=(tracks*layers)*ts1; %Duration of simulation (s)
    ts=linspace(ts1,t_end,tracks*layers);
    ts=transpose(ts);

    i=1:layers*f;
    j=1;

    Temp=zeros(1,numel(i)); %Array for Temperature
    Temp2=zeros(1,numel(j)); %Array for Temperature for Nakamura model
    N=zeros(1,numel(i)+1); %Nakamura Matrix

    %Definition of time step
    time=linspace(0.00025,t_end, layers*f);
    delta_t=time(1,3)-time(1,2);

    for i=i

        t=time(i);

        %Melt pool height (m)
```

```

h=0.08*((n*p*(rb/vx))/(pi*rb^2*sqrt(alpha*rb/vx)*...
(rho*c*Ts)))^1.4)*rb;

k=1;
delta=150;
while delta>1

    b=1;
    c=1;
    while t>ts(b)

        %If-loops defining track direction
        if mod(b,2)==0
            vx=vx;
            xs=0;
            vy=0;
        else
            vx=-vx;
            xs=vx*ts(1);
            vy=0;
        end

        %If-loops defining depth of solution domain (layer
        %dependent)
        if b>tracks
            ys=rem(b,tracks)*dy-dy;
            z=-H*(layers-1)-H*(floor(b/tracks)-(layers-1))+zs;

            if mod(z-zs,-0.00002)~=0

                xsnew=ys;
                ys=xs;
                xs=xsnew;
                vy=v;
                v=0;

            end

        else
            ys=b*dy;
            z=zs;
        end

        %Heat input per time step
        T=@(t2)1./((4*fp*alpha*(t-t2)+rb^2)...
        .*sqrt(4*fd*alpha*(t-t2)+h^2))...
        .*exp(-fp*((x-(xs+v*(t2-ts(b))))...
        .^2+(y-(ys+vy*(t2-ts(b))))).^2)...
        ./((4*fp*alpha*(t-t2)+rb^2)-((fd*z^2)...
        ./((4*fd*alpha*(t-t2)+h^2))));

        q(c)=integral(T,ts(b),t);

        c=c+1;
        b=b+1;
    end

    %Track 1
    vx=vx;
    vy=0;
    xs=0;
    ys=0;
    z=zs;

```



```

%Heat input from Track 1
T_old=@(t2)1./((4*fp*alpha*(t-t2)+rb^2)...
.*sqrt(4*fd*alpha*(t-t2)+h^2))...
.*exp(-fp*((x-(xs+v*t2)).^2+(y-(ys+vy*t2)).^2)...
./(4*fp*alpha*(t-t2)+rb^2)-((fd*z^2)...
./(4*fd*alpha*(t-t2)+h^2)));

q(c)=integral(T_old,0,t);

%Sum of heat input from all tracks
Q=sum(q)*(2*fp*n*P*sqrt(fd)*2*m)./(rho*cp0*pi*sqrt(pi));

%Temperature at point of interest
Tnew(k)=((sqrt(Q+((1+m*T0)^2)))-1)./m;

%If-loops for linearization of specific heat
if (Tnew(k)>=693 && Tnew(k)<1473)
    m=-0.000329; % Specific heat at glassy state
    cp0=777.69213;

elseif (Tnew(k)>=593 && Tnew(k)<693) % Specific heat
    % at transition state
    m=-0.002314;
    cp0=-993.9;

elseif (Tnew(k)<593)
    m=0.0002; % Specific heat at liquid state
    cp0=331.709;

else
    m=((400/331.709)-1)/Tnew(k);
    cp0=331.709;

end

if k>1
    del ta=abs(Tnew(k-1)-Tnew(k));

end

Cp(k)=cp0*(1+m*Tnew(k));

%Adjusting specific heat for convergence
if k>1 && Cp(k)>Cp(k-1)
    Cp(k)=Cp(k)-0.99*(Cp(k)-Cp(k-1));
end

m=((Cp(k)/331.709)-1)/Tnew(k);
cp0=331.709;

k=k+1;

end

Tnew=Tnew(k-1);
Temp(i)=Tnew-273;
Temp2(j)=Tnew;

%Determining degree of crystallinity using Nakamura model
if j==1

    N(j)=0;
    X(j)=0;

elseif Temp2(j)>1200

```

```

        N(j)=0;
        X(j)=0;

    else

        N(j)=N(j-1)+delta_t*Nakamura_model_2202(Temp2(j-1));

        X(j)=X(j-1)+delta_t*4*Nakamura_model_2202(Temp2(j-1))*...
            exp(-(N(j))^4)*N(j)^3;
    end

    j=j+1;

end

%Plotting of results
u=1:1:layers;

for cc = 1: numel(u)

    plot(time(1,1:f),Temp(1,(1+(f*(u(cc)-1)):f*u(cc))))
    L{cc}=strcat('Layer',num2str(u(cc)));
    legend(L)
    hold on

end

%Thermal History
xlabel('Time [s]')
ylabel('Temperature [°C]')
title('Thermal History (Multi-Track)')
hold on

%Degree of crystallinity
figure
plot(time,x*100)
xlabel('Time [s]')
ylabel('Degree of Crystallinity [%]')
title('Crystallinity (Nakamura)')

%Plotcube function
figure
Point = [x,y,xs-layers*H] ; % center point
L = [length,width,-depth] ; % cube dimensions
O = [0,0,zs] ; % Get the origin of cube so that P is at center
plotcube(L,O,.2,[1 0 0]); % use function plotcube
hold on
plot3(Point(1),Point(2),Point(3),'.k')
hold on
zmax=xs-H*layers;
vertx=[0 length length 0];
verty=[0 0 width width];
vertz=[zmax; zmax; zmax; zmax];
patch(vertx,verty,vertz,"g");
xlabel('x [m]')
ylabel('y [m]')
zlabel('z [m]')

end

end

```

9.5 Nakamura Function

```

function K = Nakamura_model_2202(Temp2)

T1=1203; %Melting Temperature (K)
if Temp2>800 && Temp2<T1

%Initialization of all required variables
f=1;
a0=3.32E-10;
n0=3.46E-5;
Dstar=10;
T0=509;
rho=6640;
M=76.6;
M_SI=0.0766;
A=1.18E27;
sigma=0.04;
R=8.314;
a=5.225E-4;
b=1.031E7;
c=6.23E-3;
d=-6.046E-7;
deltaHx=-62;
deltaHf=112;
nexp=4;
kB=1.380649E-23; %Boltzmann Constant

rs=a0/2; %Wigner Seitz radius

n=n0*exp(Dstar*T0./(Temp2-T0)); %Temperature dependant viscosity

Deff=kB*Temp2/(3*pi*n*a0); %Effective diffusion coefficient

deltaSf=deltaHf/T1; %Entropy

Cp_l=(3*R+a*Temp2+b*Temp2^2)/M_SI; %Specific heat liquid phase
Cp_x=(3*R+c*Temp2+d*Temp2^2)/M_SI; %Specific heat crystal phase
delta_Cp=Cp_l-Cp_x;

Integral_1=@(T_prime) ((a*(T_prime)+b*(T_prime)...
.^-2 -c*(T_prime)-d*(T_prime).^2));
Integral_2=@(T_prime) (((a*T_prime+b*T_prime.^-2)...
-(c*T_prime+d*T_prime.^2))./T_prime;

q=integral(Integral_1,Temp2,T1);
q2=integral(Integral_2,Temp2,T1);

q=q/M;
q2=q2/M;

%Gibbs free energy difference [KJ/Kg]
Gibbs=(deltaHf-Temp2*deltaSf-q+Temp2*q2);
Gibbs=Gibbs*M_SI; % [KJ/mol]

Gibbs_normalized=Gibbs*rho/M_SI; %[KJ/m^3]
Gibbs_normalized=Gibbs_normalized*1000; %[J/m^3]

U=f/a0*Deff*(1-exp(-Gibbs*1000/(R*Temp2))); %Growth rate

deltaGstar=(16*pi*sigma^3)/(3*(Gibbs_normalized)^2);%Nucleation barrier [J]

Iss=A*Deff*exp(-deltaGstar/(kB*Temp2)); %Steady state nucleation

```

```
k=pi/3*Iss*U^3;  
k=k^(0.25);  
else  
    k=0;  
end  
end
```

Published with MATLAB® R2022b